2015

Gas Seperation through Hollow Fiber and Spiral Wound Membranes

Mohammed Faraj Alrehili
Lehigh University

GAS SEPARATION THROUGH HOLLOW FIBER AND SPIRAL WOUND MEMBRANES

By
Mohammed Alrehili

A Thesis
Presented to the Graduate and Research Committee
Of Lehigh University
In Candidacy for the Degree of
Master of Science
In
Mechanical Engineering and Mechanics

Lehigh University
Summer 2015 Semester
June 2015

CERTIFICATION OF APPROVAL

This thesis is accepted and approved in partial fulfillment of the requirements for the Master of Science.

_____

Date

_____

Thesis Advisor, Dr. Alparslan Oztekin

_____

Chairperson of Department, Dr. Gary Harlow

CONTENTS

LIST OF FIGURE

LIST OF TABLE

ACKNOWLEDGMENT

I would like to express my deep gratitude to my master thesis advisor, Prof. Oztekin for his encouragement and assistance in researching the topic of this thesis. Also, I would like to express my sincere appreciation to my parents Aziza and Faraj Alrehili for their emotional support.

Finally, I would like to express my worm thanks and appreciation to my wife, Rana Alrehili, for her love and support and for helping me to complete my master degree, and for my beloved daughter Joanna who was always a source of unending joy.

NOMENCLATURE

A	Surface area	f_i	particle density distribution function
c	lattice speed	h	channel height
c_s	lattice sound speed	s	Collision frequency
C	concentration [mol/m^3]	L	membrane length [m]
C_D	drag coefficient	Re	Reynolds number [-]
D	diffusion coefficient [m^2/s]	Sc	Schmidt number [-]
d	HFM diameter [m]	l	thickness of membrane [m]
d_h	Hydraulic diameter of a spacer	mm	velocity moment vector
e_i	discrete lattice velocity set	mm^{eq}	equilibrium velocity moment vector
J	molar flux [mol/m^2]	$\ddot{P}$	permeability [$\frac{\text{mol}}{\text{m s Pa}}$]
M	molecular weight [g/mol]	U	average velocity [m/s]
Na	mole fraction [-]	hm	mass transfer coefficient [m/s]
P	permeance [$\frac{\text{mol}}{\text{m}^2\text{s Pa}}$]	p	pressure [Pa]
S	spacing between HFM [m]	$\beta*,\beta 1,\beta$	turbulent model parameters [-]
Sh	Sherwood number [-]	υ	kinematic viscosity [m^2/s]
Vw	suction rate [m/s]	ω	specific dissipation rate[1/s]
k	turbulent kinetic energy [J/kg]	$\boldsymbol{u}$	velocity vector
m	mass flux [kg/(s m^2)]	F_1, F_2	blending functions
u	x-component of velocity [m/s]	μ_t	eddy viscosity
x	x coordinate [m]	τ	nondimensional time
Δp	pressure difference [Pa]	ρ	density [kg/m^3]
α	mass selectivity [-]	γ	rate of strain tensor
σ,λ	turbulent model parameters [-]	St	Strouhal number
D_T	eddy diffusion coefficient	μ	dynamic viscosity
Sc_T	turbulent Schmidt number	t	time
δx	lattice width	δt	time step
w_i	weighting vector	α	selectivity
g_i	particle concentration distribution function	M	transformation matrix

Subscripts and Superscripts

a and b	species: CO_2 or CH_4	w	properties at the membrane surface
i and j	index notation	T	eddy properties
CH_4	properties of CH_4	CO_2	properties of CO_2
tot	total properties	a/b	ratio of properties of a to b

Abstract

Computational fluid dynamics simulations are conducted for multicomponent fluid flows over banks of hollow fiber membranes. The hollow fiber membrane systems is considered here for gas separation applications. Separation of carbon dioxide (CO_2) from methane (CH_4) is studied using hollow fiber membranes packed in different arrangements. The membrane surface is considered as a functional surface where the mass flux and concentration of each species are coupled and are determined as a function of the local partial pressures, the permeability, and the selectivity of the membrane. k-ω Shear Stress Transport (k-ω SST) turbulent model is employed to study the mixture flow over banks of hollow fiber membrane for values of the Reynolds number up to 1000. The flow structure around the hollow fiber membranes dominates the performance of the separation process. This study demonstrates clearly that good mixing in the bank of hollow fiber membranes enhances the separation performance. The results show that hollow fiber membrane module with staggered arrangement performs much better than that with inline arrangement. For the spiral wound membrane, it has been shown that membrane performance could be greatly enhanced by momentum mixing in the feed channel induced by spacers. Square shaped spacer will be considered in the inline arrangement for values of the Reynolds number up to 500. In order to validate the turbulence model transient flow simulations are conducted using lattice Boltzmann method. The lattice Boltzmann method to simulate flow in the geometries related to the spiral wound membrane modules is developed by our research group at Lehigh. Two dimensional nine velocity directional, D2Q9, lattice arrangement with multi-relaxation time (MRT) lattice Boltzmann method is used to simulate transient flow field while single relaxation time (SRT) lattice Boltzmann

method. Simulations are performed to determine concentration field for values of *Re* up to 300. The bounding surfaces are treated as impermeable walls for simulations conducted using the lattice Boltzmann method. The results predicted by the lattice Boltzmann method and the SST turbulence model agree well, validating the turbulence model and the numerical method.

1. Introduction

Membrane based gas separation has been successfully used in various industrial applications since it offers several advantages. It is cost effective, is easy to implement, and is energy efficient compared to conventional separation processes [1]. There are different types of flows in these membrane modules: countercurrent flows; concurrent flows and radial crossflows [2]. The present study investigates the spatial and temporal characteristics of the radial crossflows in the hollow fiber membrane modules and their effects on the membrane performances.

Several studies model only the mass balance in the hollow fiber membrane to examine membrane system performance for gas separation applications [1-4]. The effect of flow in the feed channel on the membrane performance in a spiral wound membrane module containing spacers has been studied for desalination and food processes [5-9]. Membrane surface is treated as an impermeable wall in Refs [5, 8] while Guillen and Hoek [6], Pal et al. [7] and Subramani et al. [9] considered permeable membrane surface in their studies. Anqi et al. [10] study steady and transient two dimensional flows in a feed channel containing circular shaped spacers in different arrangements. The mass flux through the membrane is modeled as a function of the osmosis pressure and the concentration. The k-ω Shear Stress Transport (SST) turbulence was employed to obtain the pressure, the concentration, and the velocity fields. Anqi et al. [10] demonstrated that the membrane performance significantly enhanced by spacers in a desalination process. Sohrabi et al. [11] consider the effect of flow over banks of hollow fiber membrane in a process separating liquid from gas. They have used predetermined velocity profile and solve just the mass transport equation to study membrane performance. Kaya et al. [12] used the k-ε

turbulence model to capture the flow over banks of hollow fiber membrane for water desalination. They concluded that characterizing flow in the feed channel should be considered in membrane simulations. However, these investigators neglect mass flux through the membrane by considering membrane surfaces as impermeable boundary. Similarly, Huang et al. [13] and Jiang et al. [14] solve the Navier-Stokes equations to study the flow over banks of hollow fiber membrane with impermeable surfaces for dehumidification processes. Real separation process in hollow fiber membrane modules requires a proper mass flux model through the membrane. Mass fluxes through the membrane should be determined as a function of the local pressure and mass fraction and membrane properties.

Alkhamis et al. [15] introduced a unique model for the mass flux through the membrane for gas separation process. The membrane wall is treated as a functional surface, where the mass fluxes of species are calculated based on the local pressure, membrane permeability and the selectivity. Alkhamis et al. [15] studied the separation CO_2 from CH_4 in a spiral wound membrane module containing spacers and concluded that separation process can be enhanced significantly by the presence of spacers in the membrane system. It has been demonstrated by these investigators that spacers should be an integral part of the membrane system design and optimization in the application of gas-gas separation. More recently, Alkhamis et al. [16] conducted computational simulations to study a gas separation process in a hollow fiber membrane containing a porous support layer. They employed the same flux model described above to investigate the effect of the porous support layer on the separation process of CO_2 in a CO_2/CH_4 mixture. It has demonstrated that the presence of the porous layer has profound adverse effects on the hollow fiber

membrane performance. Mass flux of both CH_4 and CO_2 is reduced by the presence of the porous layer. Alkhamis et al. [17] showed that flow restricting devices such as orifices can be utilized to alleviate undesirable effects of the porous support layer on the membrane performance.

In this study, the membrane flux model proposed by the present authors [15-17] is employed to study membrane performance in a separation module containing bundles of hollow fiber membranes. The present work utilizes CFX commercial software to simulate steady two dimensional velocity and concentration fields to investigate the effect of momentum mixing in the feed channel on the hollow fiber membrane performance. A binary mixture of methane (CH_4) and carbon dioxide (CO_2) is considered as fluid flowing over hollow fiber membrane banks. Flow simulations are conducted for a wide range the Reynolds numbers, $200 \leq Re \leq 1000$. Spatial characteristics of the cross flow over a bank of hollow fiber membrane with an inline and staggered arrangements are simulated using the k-ω Shear Stress Transport (k-ω SST) turbulence models. Turbulence model and the numerical method are validated by comparing the predicted values of the drag coefficient and the Strouhal number for flows past a cylinder against those documented in the literature.

For spiral wound membrane, square spacers will be considered in inline arrangement for Re = 300 and 500 inside channel bounded by two parallel spiral wound membranes. In a channel without spacers, the steady flow is characterized by a laminar flow model. In a channel containing spacers, the Shear Stress Transport (SST) k-ω turbulence model is employed to simulate the flow field. The present authors documented that the shape and arrangements of spacers have profound influence on the membrane

performance in spiral wound membrane modules containing circular and triangular spacers in inline and staggered arrangements [15-16]. The present study focuses on improving membrane performance using momentum mixing by placing square cross-sectioned spacers in the feed channel. Enhancing turbulence to improve membrane performance has been studied extensively in the context of Reverse Osmosis [8-9, 18-24]. These studies investigated the effect of the momentum mixing without utilizing the mass transport equation. Karode and Kumar [18] study steady three dimensional laminar flow in a channel containing cylindrical spacers. Bounding surfaces in their study was impermeable and there was no mass flux through which. Wiley and Fletcher [19] and Villaluega and Cohen [20] have been calculated mass flux through a membrane from the local concentration for flows inside channel without spacers. Ma et al. [21] studied laminar flows in a channel bounded by two parallel membrane. The channel contained uniformly spaced square spacers. It was demonstrated that the average permeate flux could be significantly improved by the presence of spacers. Fimbres-Weihs et al. [22] and Subramani et al. [9] studied laminar flows in channels containing circular spacers. Fimbres-Weihs and Wiley [23] and Shkaib et al. [8] have studied three dimensional laminar flows inside channel between two parallel membranes.

Lattice Boltzmann method (LBM) is shown to be an effective computational tool to simulate complex flows [25-26]. It has been successfully applied to model isothermal and non-isothermal flows with the limitations of numerical instabilities [27-28]. This method could be considered as a special discretization of Boltzmann equation. Successive collision and propagation steps are utilized to iteratively calculate the velocity and the concentration field. Collision operation can be carried out using different approaches, i.e.

the velocity space relaxation resulting in single relaxation time (SRT) and the moment space relaxation resulting in multi relaxation (MRT) [29-30]. The lattice Boltzmann method is developed by a researcher in our group and is employed here to help validating the turbulence model and the numerical method employed. The lattice Boltzmann method can also be effectively used to study the transient effect on the membrane performance.

2. Hollow fiber membrane model

The schematic of the flow geometry is illustrated in Figure 1. It consists of arrays of hollow fiber membrane with an inline and a staggered arrangement. The diameter of hollow fiber membrane is d, the length of the membrane module is $L = 50d$, and the spacing between two consecutive hollow fiber membrane is S. The inline and staggered arrangement of the hollow fiber banks with the spacing S/d of 2 and 2.5 are considered. The height of the hollow fiber bundle, h, is $12d$ for banks with $S/d = 2$ and is $15d$ for banks with $S/d = 2.5$. The distance $6d$ is assigned between the inlet and the bank of hollow fiber membrane. The distance between the outlet and the hollow fiber membrane bank is $28d$ for $S/d = 2$ while it is $24d$ for $S/d = 2.5$. The length of the inlet and outlet regions are selected such that the effect of the boundary conditions imposed at the inlet and the outlet have minimal influence on the flow structure in the bank of the hollow fiber membranes. The physical properties of the binary mixture of CH_4 and CO_2 are assumed to be constant. The flow is isothermal and incompressible. The diffusion coefficient is assumed to be independent of the concentration. Steady state simulations for banks of circular cross-sectioned hollow fiber membranes are conducted for the Reynolds numbers up to 1000. Moreover, a transient simulation at $Re = 200$ is conducted using the k-ω Shear Stress

Transport (k-ω SST) turbulent model for validation in flows over a single circular cylinder that has an impermeable surface.

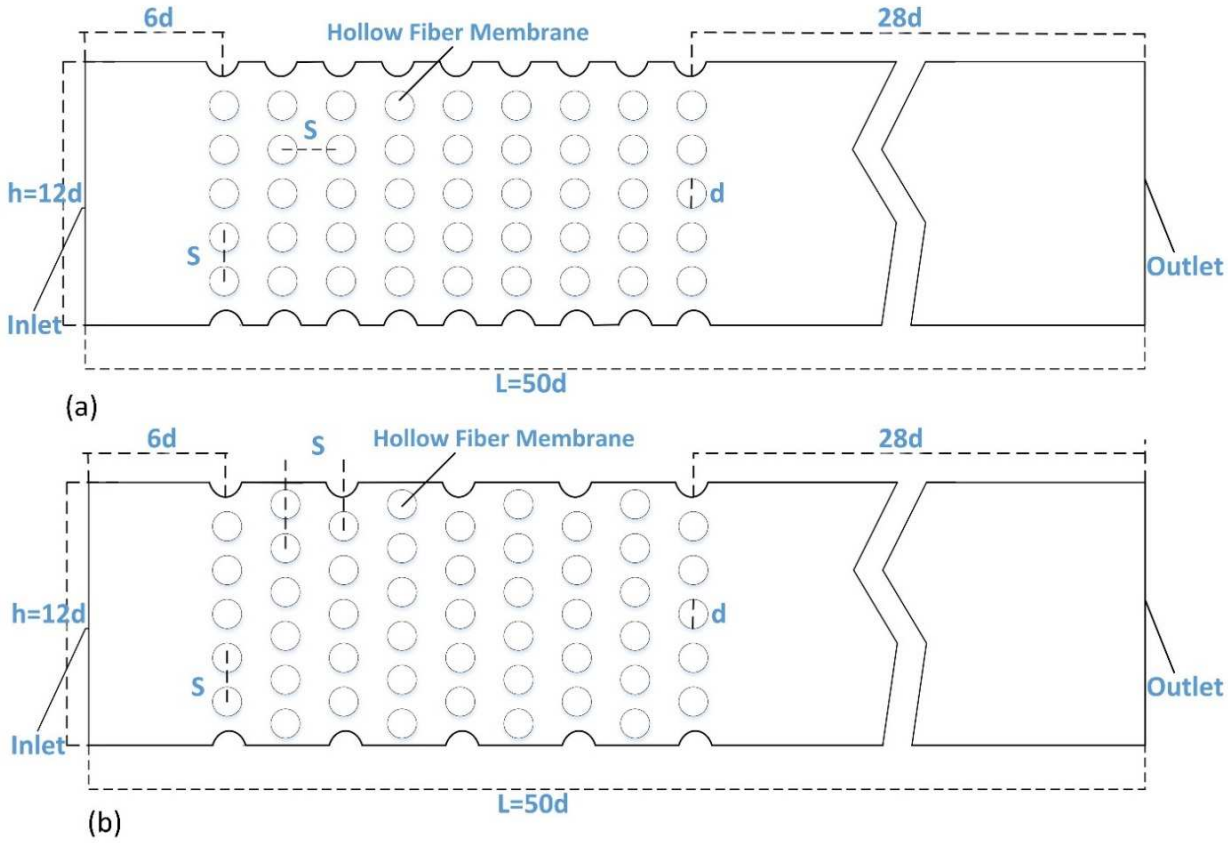

Figure 1: The schematic of the (a) inline geometry and (b) staggered geometry for *S/d* = 2. The inlet region, the outlet region and the bank of the hollow fiber membranes are shown with dimensions.

The binary mixture of CH_4 and CO_2 is assumed to be incompressible and Newtonian fluids with constant density (ρ), dynamic viscosity (μ) and mass diffusion coefficient (D).

At the inlet, uniform velocity and mole fraction profiles are applied while at the outlet, zero pressure and zero gradient boundary condition is applied. Periodic boundary condition is applied at the side boundaries of the computational domain to model an

infinitely wide hollow fiber membrane bank region. A detailed description of the membrane model and the boundary conditions is given later in this chapter.

3. Spiral Wound Membrane model

Steady two dimensional flows of CH_4 and CO_2 binary mixture in a channel containing spacers are studied using k-ω Shear Stress Transport turbulence model for Re = 300 and 500. The Reynolds numbers is defined as $Re = Uh/\nu$, where ν is kinematic viscosity, U is the average velocity at the inlet, and h is the channel height. The aspect ratio of the computational domain is 120 (L/h). Seventeen square cross-sectioned spacers are placed in inline arrangement at the mid-plane between the membranes as shown in

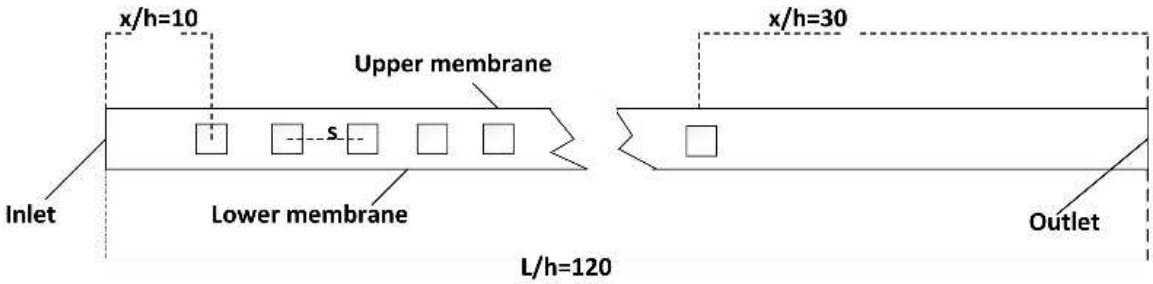

Figure 2: The schematic of the membrane module containing an array of spacers

At the inlet, the fully developed flow is considered. On the surface of the membrane, the no-slip boundary condition is imposed on the velocity field with the suction rate determined from local pressure and concentration. At the exit, the zero gradient conditions are applied. Boundary conditions imposed on the velocity and concentration field are described in detail below.

This objective of simulations conducted for this geometry illustrated in Figure 2 is to validate the turbulence model and the numerical model employed for simulations conducted for hollow fiber membrane module.

4. Governing Equations

The equations governing the fluid motions and mass transfer are:

the continuity

$$\frac{\partial u_i}{\partial x_i} = 0, \tag{1}$$

the conservation of momentum

$$\frac{\partial u_i}{\partial t} + u_j \frac{\partial u_i}{\partial x_j} = -\frac{1}{\rho}\frac{\partial p}{\partial x_i} + \frac{1}{\rho}\frac{\partial}{\partial x_j}\left(\mu \frac{\partial u_i}{\partial x_j}\right), \tag{2}$$

and the mass transport equation of species "a"

$$\frac{\partial CN_a}{\partial t} + u_j \frac{\partial CN_a}{\partial x_j} = \frac{\partial}{\partial x_j}\left(D \frac{\partial CN_a}{\partial x_j}\right). \tag{3}$$

Here i = 1,2. j is the summation index, $u_1 = u$ is the stream-wise component of the velocity and $u_2 = v$ is the span-wise component of the velocity, $x_1 = x$ and $x_2 = y$ are the spatial coordinates, t is time, ν is kinematic viscosity ($\nu = \mu/\rho$) and p is pressure. $C = C_a + C_b$ is the concentration of the binary mixture, Ca is the concentration of species "a", C_b is the concentration of species "b". Na = Ca/C is the mole fraction of species "a".

4.1 Turbulence modeling

The present authors [10] successfully employed k-ω Shear Stress Transport (k-ω SST) turbulence model to characterize flows in the feed channel of a spiral wound membrane module containing spacers. They have conducted computational fluid dynamics simulations for the range of Re from 400 to 4000 in a desalination process. k-ω SST

turbulence model proposed by Menter [31] is also utilized in the present work to simulate flows past arrays of hollow fiber membrane. The turbulence model can predict the turbulent flow structure near boundaries and the inception of flow separation accurately. With the eddy viscosity defined as $\mu_t = \rho \frac{a_1 k}{\max(a_1 \omega; \Omega F_2)}$ the equations for k-ω SST turbulence model yields

$$\frac{\partial u_i}{\partial t} + u_j \frac{\partial u_i}{\partial x_j} = -\frac{1}{\rho}\frac{\partial p}{\partial x_i} + \frac{1}{\rho}\frac{\partial}{\partial x_j}\left((\mu + \mu_t)\frac{\partial u_i}{\partial x_j}\right) \tag{4}$$

The equations governing the turbulent kinetic energy, *k,* and the specific dissipation rate, *ω*

$$\frac{\partial(\rho k)}{\partial t} + u_i \frac{\partial(\rho k)}{\partial x_i} = \tau_{ij}\frac{\partial u_i}{\partial x_j} - \beta^* \rho \omega k + \frac{\partial}{\partial x_j}\left[(\mu + \sigma_{k1}\mu_t)\frac{\partial k}{\partial x_j}\right] \tag{5}$$

$$\frac{\partial(\rho \omega)}{\partial t} + u_i \frac{\partial(\rho \omega)}{\partial x_i} = \frac{\gamma}{\nu_t}\tau_{ij}\frac{\partial u_i}{\partial x_j} - \beta \rho \omega^2 + \frac{\partial}{\partial x_j}\left[(\mu + \sigma_\omega \mu_t)\frac{\partial \omega}{\partial x_j}\right] + 2\rho(1 - F_1)\sigma_{\omega 2}\frac{1}{\omega}\frac{\partial k}{\partial x_j}\frac{\partial \omega}{\partial x_j} \tag{6}$$

The equation governing the mass transport of species "a" for the turbulent flow is

$$\frac{\partial CN_a}{\partial t} + u_j \frac{\partial CN_a}{\partial x_j} = \frac{\partial}{\partial x_j}\left((D + \sigma D_T)\frac{\partial CN_a}{\partial x_j}\right) \tag{7}$$

where Ω is the vorticity magnitude, $a_1, \beta, \beta^*, \sigma_{k1}, \sigma_\omega, \sigma_{\omega_2}$ are closure coefficients. β is selected to be 0.09. D_T is the eddy diffusion coefficient and $Sc_T = \upsilon_T / D_T$ is the turbulent Schmidt number. Sc_T is selected to be 0.85. Detailed description of the turbulence model parameters are given in Ref [17].

4.2 Membrane Modeling and Boundary Condition

Following the approach proposed by the present authors [15-17] the boundary conditions imposed on the velocity and the concentration field along the surface of the membranes are determined from the first principles. The molar flux of the species "a" across the membrane per unit area, *J*a, extracted from the feed flow is determined as

$$J_a = \frac{\ddot{P}_a}{l}\left(p_a^{(1)} - p_a^{(2)}\right) = \frac{\ddot{P}_a}{l}\Delta p_a \tag{8}$$

where l is the thickness of the membrane, $\ddot{P}_a$ is the molar permeability of species "a", and $\Delta p_a = \left(p_a^{(1)} - p_a^{(2)}\right)$ is the partial pressure difference of species "a" across the membrane. Then the total molar flux (J) per unit area through the membrane can be determined as

$$J = J_b + J_a = \Delta p_b \frac{\ddot{P}_b}{l} + \Delta p_a \frac{\ddot{P}_a}{l} \tag{9}$$

Equation (9) can be rewritten in terms of molar selectivity,$\alpha = \ddot{P}_a/\ddot{P}_b$, as

$$J = \frac{\ddot{P}_b}{l}\left[\Delta p_{tot}\alpha + \Delta p_b(1-\alpha)\right] \tag{10}$$

where J_a and J_b are molar flux of species of "a" and "b", $\Delta p_{tot} = \Delta p_b + \Delta p_a$ is the total pressure difference through the membrane. The membrane selectivity is defined as $\alpha = \ddot{P}_a/\ddot{P}_b = P_a/P_b$ where $P_a = \frac{\ddot{P}_a}{l}$ and $P_b = \frac{\ddot{P}_b}{l}$ are permeance of species "a" and "b", respectively. Equation (7) also uses the relationship between the total pressure and the partial pressure of species: $\Delta p_a = N\text{a}\,\Delta p_{tot}$ equation (9) yields

$$J = \Delta p_{tot} P_b\left[Y_b(1-\alpha) + \alpha\right] \tag{11}$$

With the definition $Vw = J/C$, the suction rate, V_w, can be calculated as

$$V_w = \frac{\Delta p_{tot} P_b}{C} [N_b(1-\alpha) + \alpha] \quad (12)$$

The suction rate along the membrane surfaces is shown to be a function of the selectivity of the membrane, the permeability of the membrane, the total pressure drop across the membrane, and the local mass fractions of the species. The boundary conditions imposed on the velocity field at the surface of membrane is no slip ($u = 0$) and the suction ($v = V_w$). The boundary conditions at the surface of the membrane imposed on the concentration field is obtained from the conservation of mass

$$J_a = -D \frac{\partial C_a}{\partial r} = -D \frac{\partial}{\partial r}(CN_a) \quad (13)$$

where *Ca* is the concentration of species "*a*". Accounting for the concentration variation and utilizing equation (8) the boundary condition for the mole fraction of species "*a*" along the surface of membrane is derived as

$$\frac{\partial N_a}{\partial r} = \frac{\partial}{\partial r}\left(\frac{C_a}{C_b + C_a}\right) = \frac{1}{C^2}\left((C_b + C_a)\frac{\partial C_a}{\partial r} - C_a \frac{\partial}{\partial r}(C_b + C_a)\right) = \frac{1}{C^2}\left(C_b \frac{\partial C_a}{\partial r} - C_a \frac{\partial C_b}{\partial r}\right) \quad (14)$$

As shown in equation (14) the variation in total density is accounted for. Using $J_a = -D \frac{\partial C_a}{\partial r} = -D \frac{\partial}{\partial r}(CN_a)$ and equation (14) the boundary condition for the mass fraction of species "*a*" along the surface of membrane is

$$D \frac{\partial N_a}{\partial r} = \frac{1}{C^2}\left(C_b D \frac{\partial C_a}{\partial r} - C_a D \frac{\partial C_b}{\partial r}\right) = \frac{1}{C^2}(C_a J_b - C_b J_a) \quad (15)$$

Using the definition of mole fraction equation (15) can written as

$$D \frac{\partial N_a}{\partial r} = \frac{1}{C}\left(\frac{C_a}{C} J_b - \frac{C_b}{C} J_a\right) = \frac{1}{C}(N_a J_b - N_b J_a) \quad (16)$$

Using the molar flux through the membrane given in equation (16)

$$J_a = \Delta p_a P_a \quad \text{and} \quad J_b = \Delta p_b P_b, \quad (17)$$

Equation (16) yields

$$D\frac{\partial N_a}{\partial r} = \frac{1}{C}(N_a \Delta p_b P_b - N_b \Delta p_a P_a) \quad (18)$$

Utilizing the definition of selectivity and partial pressure ($\alpha = P_a/P_b$) the boundary condition for the molar fraction at the surface of the membrane can be written as

$$D\frac{\partial N_a}{\partial r} = \frac{1}{C}(N_b \Delta p_a P_a - N_a \Delta p_b P_b) = \frac{P_b \Delta p_{tot}}{C}(1-\alpha) N_b N_a \quad (19)$$

The diffusive flux at the surface of the membrane is equated to the intrinsic rejection

$$-D\frac{\partial C_a}{\partial r} = R V_w C_a \quad (20)$$

The rejection rate can then be written as

$$R = \frac{\alpha}{\alpha + (1-\alpha)N_b} \quad (21)$$

The detailed derivation of the suction rate and the flux condition applied at the surface of the is provided in [16].

The diffusion coefficient for CO_2 and CH_4 is 1.9x10^{-6} m^2/s. The mole fraction of CH_4 at the inlet is selected to be 0.7. The permeance of the membrane is P_{CO_2} = 9.8x10^{-6} $mole/m^2 s\ Pa$ and the membrane selectivity is $\alpha = P_{CH_4}/P_{CO_2}$ = 0.0086. Schmidt number is selected as 1.5 and a total pressure difference across the membrane is selected as Δp_{tot} = 7 MPa for all the results presented

4.3 Lattice Boltzmann method

Lattice Boltzmann method solves the Navier-Stokes equation with small velocity expansion. It solves microscopic kinetic equation for particle distribution to obtain macroscopic velocity and density.

SRT and MRT approach has been used to simulate concentration and velocity fields, respectively.

The MRT approach is expressed as

$$f_i(\vec{x} + \vec{e}_i\delta t, t + \delta t) = f_i(\vec{x}, t) - M^{-1} \cdot \hat{S} \cdot \left[m_i(\vec{x}, t) - m_i^{eq}(\vec{x}, t)\right], \quad (22)$$

where f_i is particle density distribution function at the velocity direction $\vec{e}_i$. M matrix transforms distribution functions f to the velocity moments mm. $\hat{S}$ is diagonal collision matrix defined by

$$S = [s_0, s_1, s_2, s_3, s_4, s_5, s_6, s_7, s_8] \text{ and } \hat{S} = I \cdot S \quad (23)$$

The collision frequencies are

$$S = [1 \quad 1.4 \quad 1.2 \quad 1 \quad 1 \quad 1 \quad 1 \quad 1.58 \quad 1.58] \quad (24)$$

Transformation between velocity space and moment space is expressed as

$$mm = M \cdot f \text{ and } f = M^{-1} \cdot mm \quad (25)$$

The coefficients of the transformation matrix are

$$M = \begin{bmatrix} 1 & 1 & 1 & 1 & 1 & 1 & 1 & 1 & 1 \\ -4 & -1 & -1 & -1 & -1 & 2 & 2 & 2 & 2 \\ 4 & -2 & -2 & -2 & -2 & 1 & 1 & 1 & 1 \\ 0 & 1 & 0 & -1 & 0 & 1 & -1 & -1 & 1 \\ 0 & -2 & 0 & 2 & 0 & 1 & -1 & -1 & 1 \\ 0 & 0 & 1 & 0 & -1 & 1 & 1 & -1 & -1 \\ 0 & 0 & -2 & 0 & 2 & 1 & 1 & -1 & -1 \\ 0 & 1 & -1 & 1 & -1 & 0 & 0 & 0 & 0 \\ 0 & 0 & 0 & 0 & 0 & 1 & -1 & 1 & 1 \end{bmatrix} \quad (26)$$

Macroscopic variables are obtained from following equations.

$$\rho = \sum_i f_i \quad (27)$$

$$\vec{u} = \frac{1}{\rho}\sum_i \vec{e}_i f_i \quad (28)$$

Discrete velocities are defined by

$$e_i = c \begin{bmatrix} 0 & 1 & 0 & -1 & 0 & 1 & -1 & -1 & 1 \\ 0 & 0 & 1 & 0 & -1 & 1 & 1 & -1 & -1 \end{bmatrix} \quad (29)$$

The kinematic viscosity of the fluid is

$$\nu = \left(\frac{1}{s_7} - \frac{1}{2}\right) c_s^2 \delta t = \left(\frac{1}{s_8} - \frac{1}{2}\right) c_s^2 \delta t, \quad (30)$$

where $c_s = c/\sqrt{3}$ is lattice speed of sound and $c = \delta x/\delta t$ is the lattice speed. Here δx and δt are lattice width and time step, respectively. The concentration field is calculated by using SRT lattice Boltzmann method.

The SRT approach can be expressed as

$$g_i(\vec{x} + \vec{e}_i\delta t, t + \delta t) = g_i(\vec{x}, t) - \frac{1}{\tau_g}\left[g_i(\vec{x}, t) - g_i^{eq}(\vec{x}, t)\right], \quad (31)$$

where g_i is particle concentration distribution function on the velocity direction $\vec{e}_i$ and τ_g is the dimensionless relaxation time. The macroscopic variables are defined as

$$N_a = \sum_i g_i \quad (32)$$

where N_a is mole fraction of species "a"

The equilibrium concentration distribution function is given by the following function

$$g_i^{eq} = w_i N_a \left[1 + \frac{3\vec{e}_i\cdot\vec{u}}{c^2} + \frac{9(\vec{e}_i\cdot\vec{u})^2}{2c^4} - \frac{3\vec{u}\cdot\vec{u}}{2c^2}\right], \quad (33)$$

where w_i is a weighting factor.

Weighting vectors for D2Q9 lattice scheme is defined as

$$w_i = \begin{cases} 4/9 & \text{for} \quad i = 0 \\ 1/9 & \text{for} \quad i = 1,2,3,4 \\ 1/36 & \text{for} \quad i = 5,6,7,8 \end{cases} \quad (34)$$

Zou-He [32] type boundary condition is employed to determine hydrodynamic properties while a boundary condition proposed in Ref [33] is used to calculate concentration values on boundaries.

5. Results and Discussions

5.1 Hollow fiber membrane

The performance of the hollow fiber membrane module will be assessed by determining the mass transfer coefficient of the hollow fiber membrane and the frictional

losses through the hollow fiber bank. The mass transfer coefficient, h_m, the corresponding local Sherwood number, *Sh*, and the average friction factor, *f*, are determined from

$$h_m(x) = \frac{D\frac{\partial N_a}{\partial y}}{(N_m - N_w)}, Sh = \frac{h_m d}{D} \text{ and} f = \frac{2d}{\rho U^2}\frac{\Delta p}{L} \quad (35)$$

Here N_m is the bulk mole fraction, N_w is the mole fraction at the wall, Δp is the pressure drop across the hollow fiber bank, and *L* is the length of the membrane bank.

Transient two dimensional simulations utilizing k-ω (SST) turbulence models are conducted at *Re* = 200 with and without suction at the boundary of the cylinders. Drag coefficients and Strouhal number without suction are compared against well documented predictions [34] and measurements [35]. Our results agree well with these previous results, as illustrated in Table 1; validating the turbulence model used in the present study. Drag coefficient is defined $C_D = 2\ F_D/\rho A U^2$ and the Strouhal number is defined by $St = fU/d$. Here F_D is the component of the force exerted by the fluid on the cylinder in the stream-wise direction, *A* is the area of the cylinder projected normal to the flow, *U* is the average velocity at the inlet and *f* is the frequency of the shedding. F_D is determined by integrating pressure and the frictional forces along the surface of the cylinder.

$Re = 200$

	C_D	*St*
Present	1.34	0.197
Glowinski[34]	1.36	0.198
Henderson[35]	1.34	0.197

Table1: Drag coefficient and the Strouhal number for flows pass an impermeable cylinder. Results predicted by the turbulence model utilized here are compared against those documented in Refs [34,35] .

When the cylinder is modeled as a hollow fiber membrane the drag coefficient and the Strouhal number are determined to be 1.3 and 0.184, respectively. They are very similar to those for flows past impermeable cylinder, as listed in Table 1. This demonstrates that flow structure in the bank of hollow fiber membranes is dominated by the vortex shedding. The Karman vortex street is not influenced strongly by the suction along the surface of the hollow fiber membrane since the intensity of the suction is not strong enough.

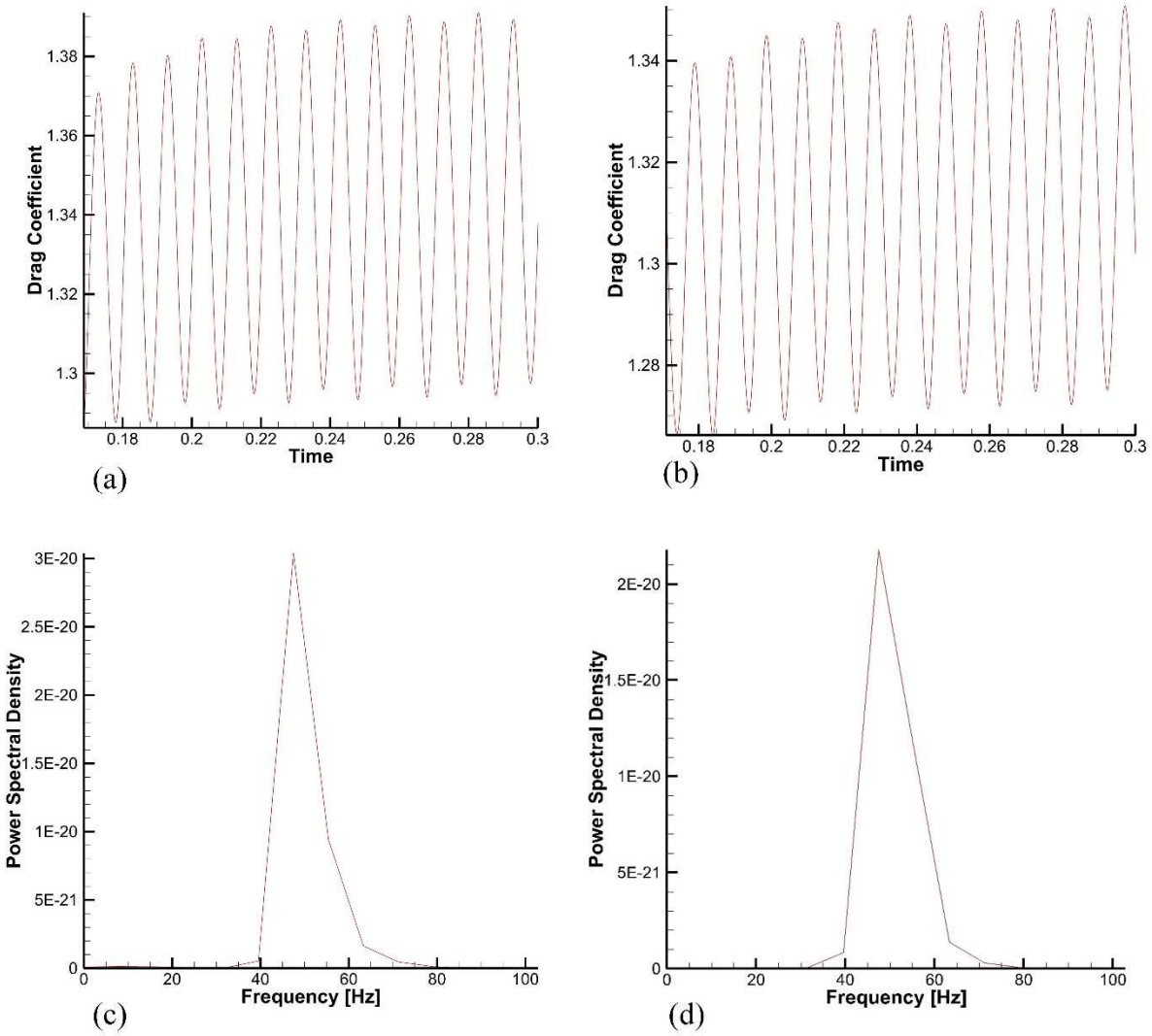

Figure 3: Drag coefficient (a,b) as a function of time and the power spectral density of the drag coefficient (c,d) at *Re* = 200 for flow past (a,c) an impermeable cylinder and (b,d) a hollow fiber membrane.

Steady state velocity and concentration field are characterized in hollow fiber banks using k-ω SST turbulence model. The hollow fibers are structured with an inline and a staggered arrangement. The hollow fiber membrane is treated as a functional permeable surface. The species permeates through the membrane at a rate that varies with the local

concentration. Simulations are conducted for values of the Reynolds number up to 1000. The Reynolds number is defined based on the hydraulic diameter of the hollow fiber membrane and the average fluid speed at the inlet, $Re = Ud/v$.

Figure 3 depicts steady state contours of the velocity field and the mole fraction of CH_4 for Re = 600 and S/d = 2. Images are acquired for both inline and staggered arrangements of hollow fiber membranes in the bank. It is noted that there are two distinct flow types in the inline geometry: jet-like flows and wake flows. Jet-like flows are obtained in the region between rows of hollow fiber membranes and wake flows are obtained in the region behind hollow fiber membranes. This creates flows similar to flow past stacks of cavities. Concentration field follows the same pattern: in the jet flow region nearly uniform low concentration of CH_4 is obtained while higher concentration is obtained in the wake region, as depicted in Figure 3. Obviously, mixing in the hollow fiber bank is not strong and this is reflected in the concentration profiles. In the staggered geometry straight jet-like flow region is not present, high speed flow surrounds the hollow fiber membrane. Wake flow region behind each hollow fiber becomes smaller and is attached to the hollow fiber membrane. Concentration distribution is more uniform in the staggered geometry compared to that in the inline geometry, as seen in Figure 3. There is a higher level of momentum mixing in the staggered geometry. The mixture becomes gradually CH_4 rich in the stream-wise direction. The concentration in the wake region is slightly elevated. There is a high level concentration polarization near the region where flow separates and the boundary layer detached from the surface of the hollow fiber membranes. The concentration polarization may not be significant for the gas separation process, but it is extremely important in the desalination process. It is well-known that concentration

polarization over the membrane surfaces influences the performance of the hollow fiber membranes adversely in the desalination process. Better mixing in the hollow fiber bank in the staggered geometry is expected to enhance hollow fiber membrane performance.

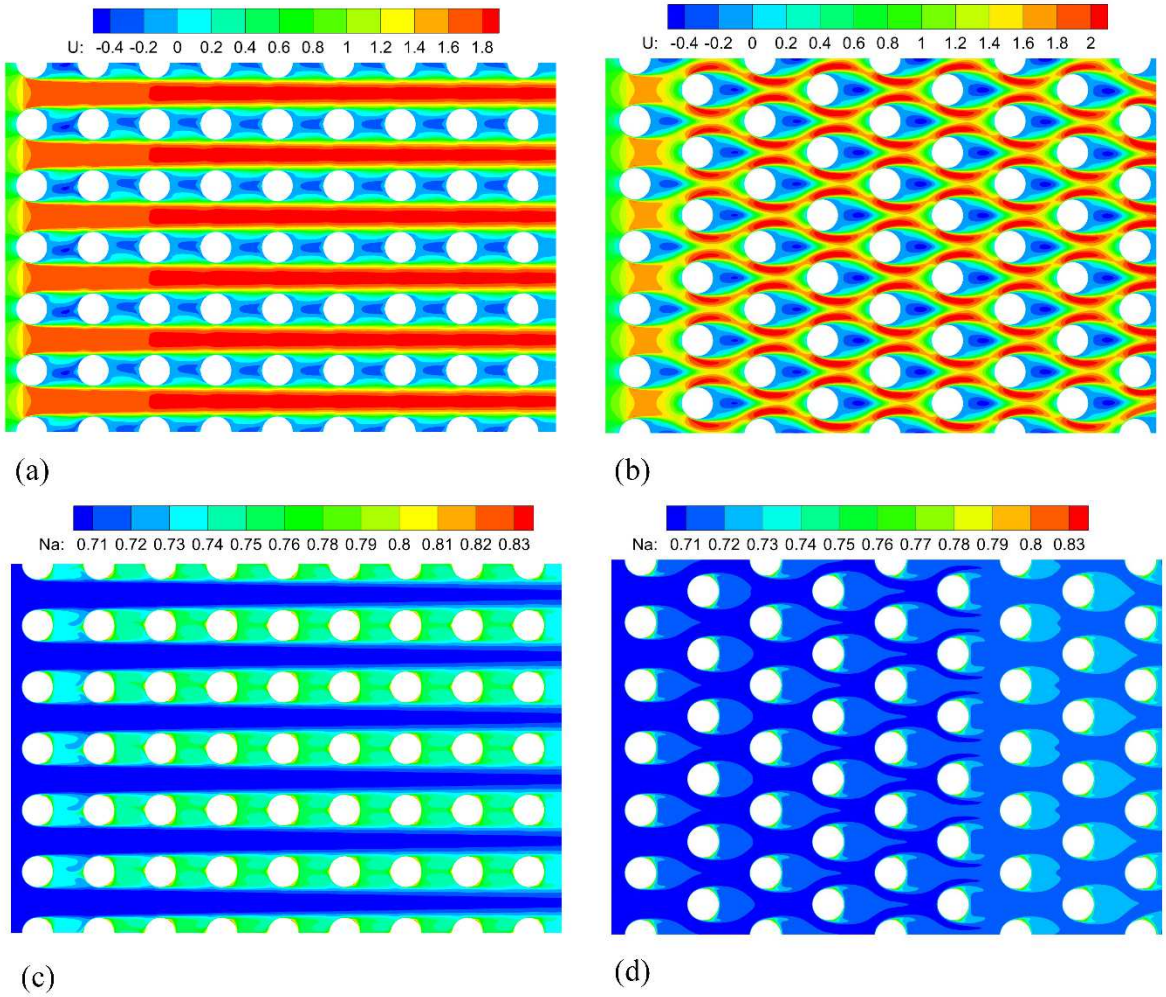

Figure 4: The contours of velocity and concentration for *Re* = 600 and *S/d* = 2. Velocity contours (a) in the inline geometry and (b) in the staggered geometry. Contours of mole fraction of CH4 (c) in the geometry and (d) in the staggered geometry.

Velocity and concentration field are shown near two hollow fiber membranes for Re = 200 and 1000 and for *S/d* = 2 and 2.5. Representative hollow fiber membranes are illustrated in Figure 5.

Velocity and concentration contours in the region near AL and AW hollow fiber membrane are depicted. Figure 6 and Figure 7 shows velocity contour at *Re* = 200 and *Re* = 1000, respectively, for flows over a staggered arrangement of hollow fiber membrane bank with *S/d* = 2. The spatial structure of the flow is very similar near these membranes with slight alterations. Similarly Figure 8 and Figure 9 shows velocity contour at *Re* = 200 and *Re* = 1000, respectively, for flows over a staggered arrangement of hollow fiber membrane bank with *S/d* = 2.5. Flow patterns are repeated around the hollow fiber membranes, as indicated in Figures 6-9.

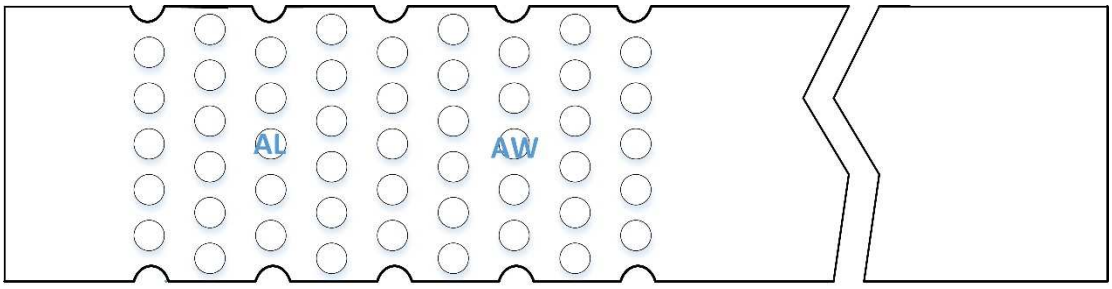

Figure 5: The schematic of hollow fiber bank illustrating selected hollow fiber membranes labelled as AL and AW

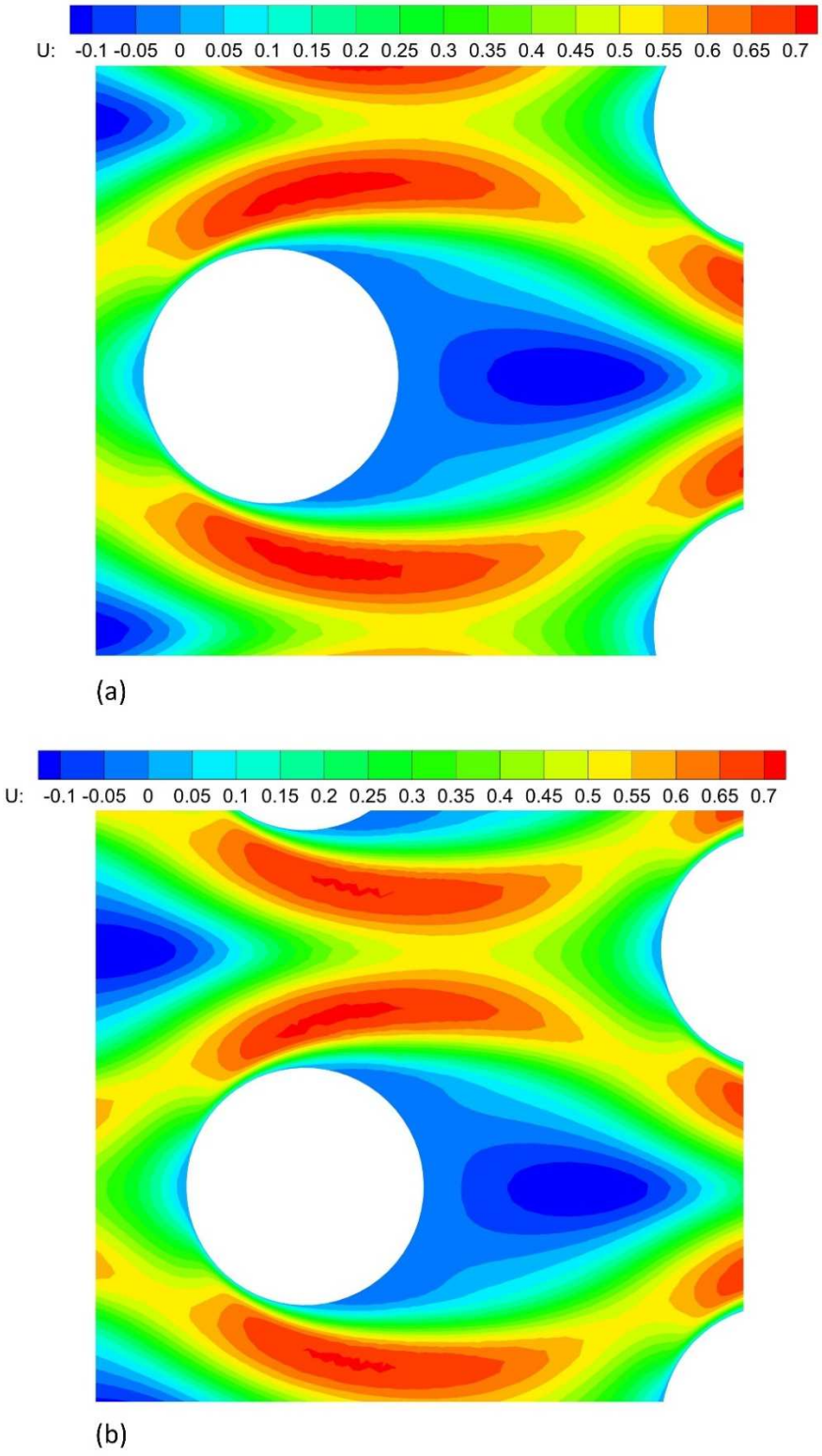

Figure 6: Velocity contours in the staggered geometry for *Re* = 200 and *S/d*=2 near two hollow fiber membranes: (a) AL and (b) AW.

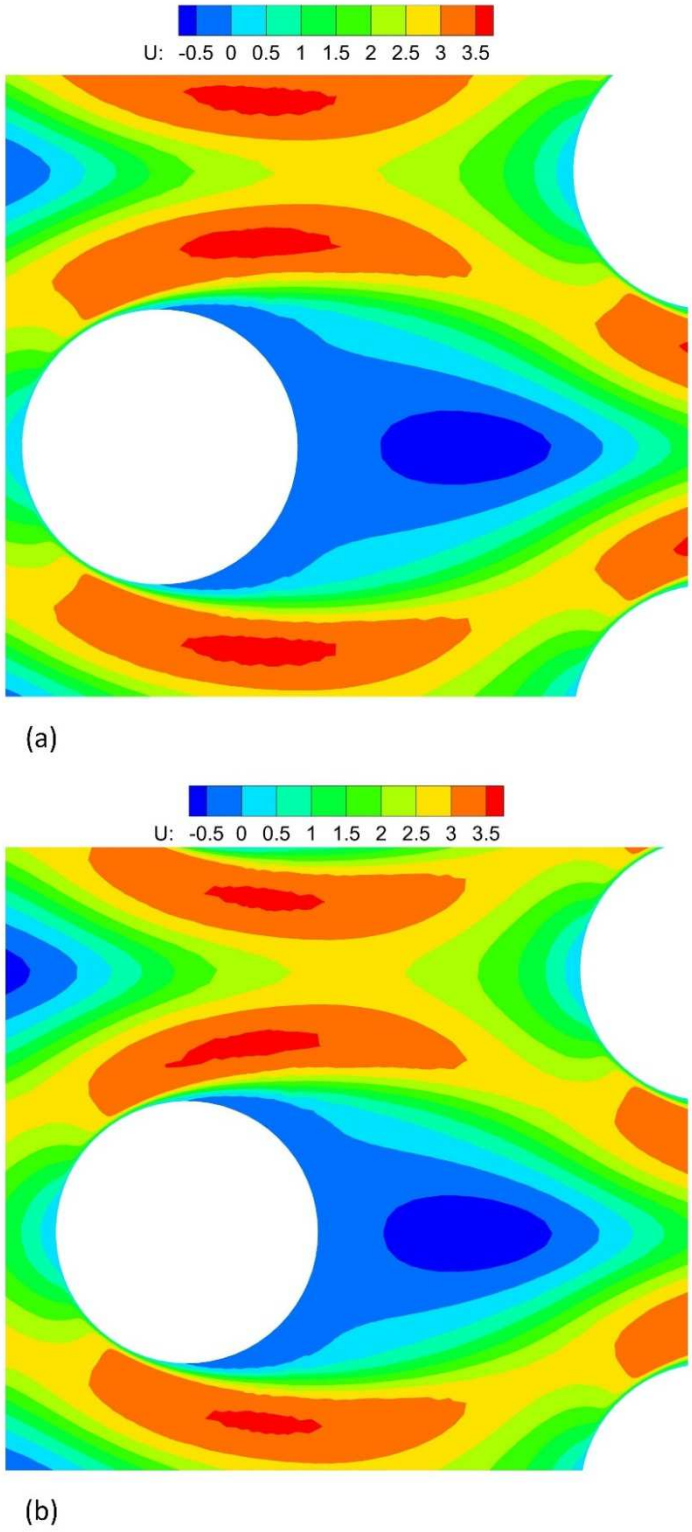

Figure 7: Velocity contours in the staggered geometry for *Re* = 1000 and *S/d*=2 near two hollow fiber membranes: (a) AL and (b) AW.

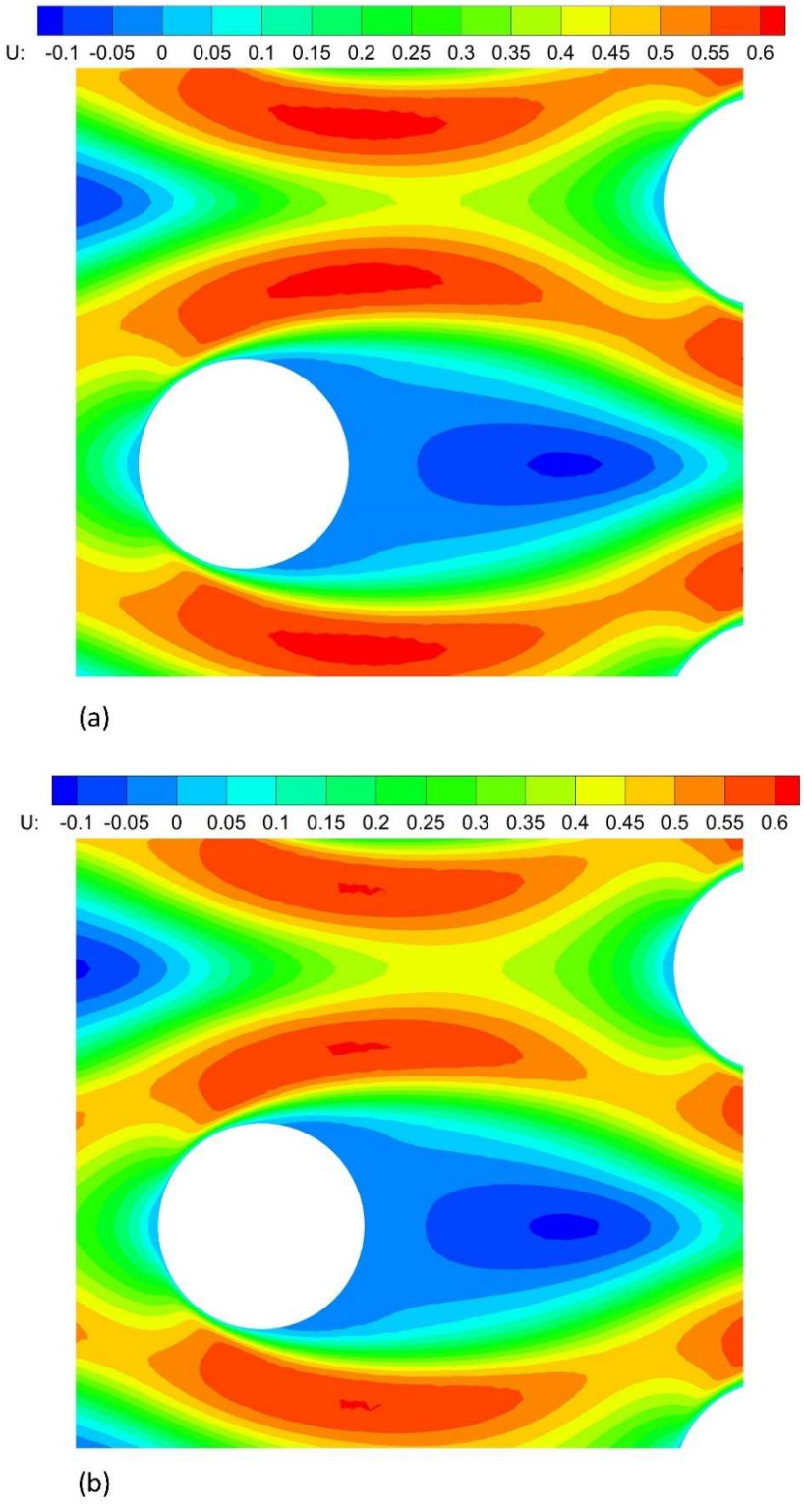

Figure 8: Velocity contours in the staggered geometry for *Re* = 200 and *S/d*=2.5 near two hollow fiber membranes: (a) AL and (b) AW.

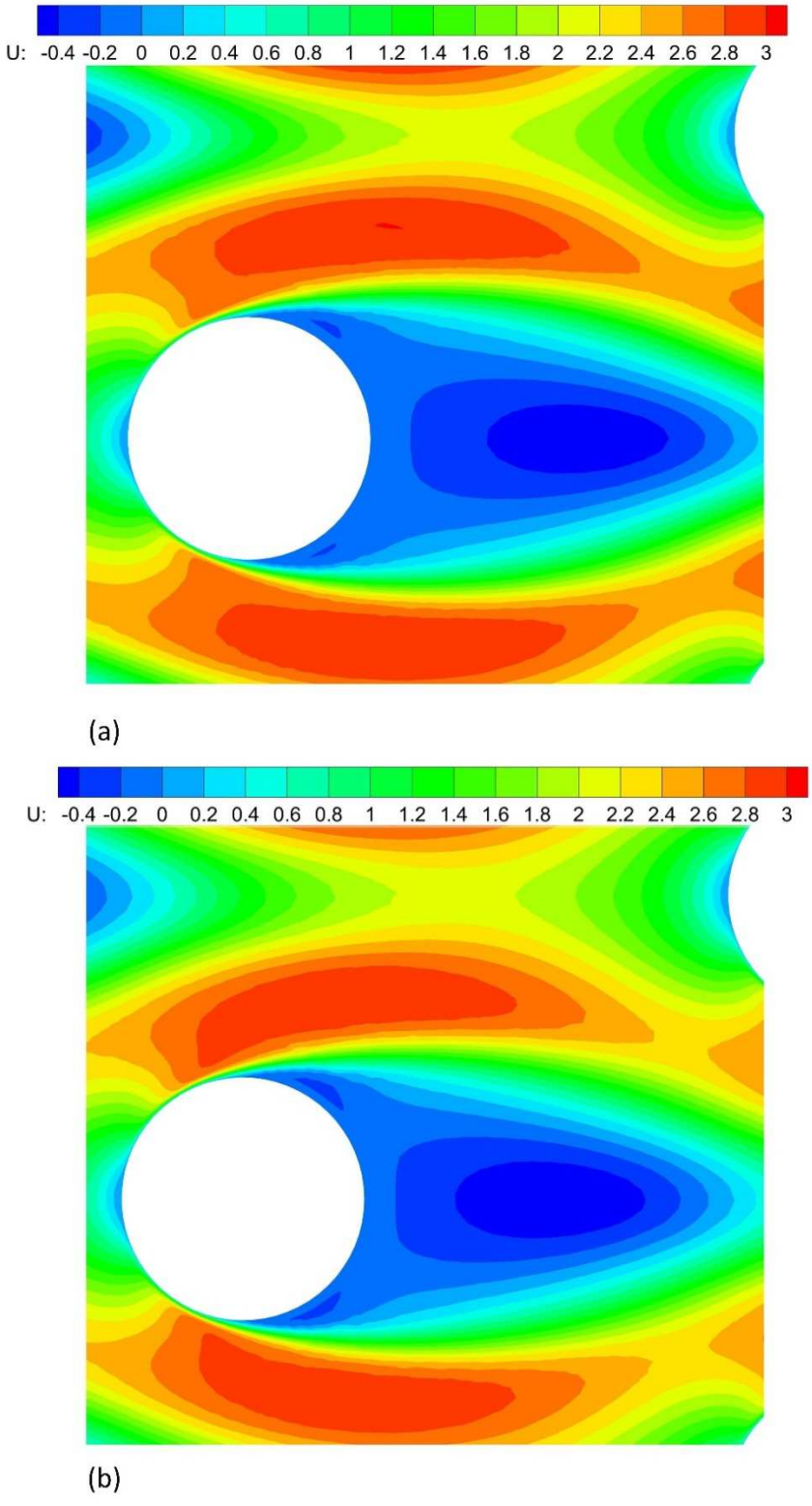

Figure 9: Velocity contours in the staggered geometry for *Re* = 1000 and *S/d*=2.5 near two hollow fiber membranes: (a) AL and (b) AW.

Figure 10 and Figure 11 illustrate mole fraction contours around hollow fibers near the inlet and the exit of the hollow fiber bank at Re = 200 and 1000, respectively, for the staggered geometry with S/d = 2. The characteristics of the concentration profiles near the hollow fiber membranes are similar at upstream and at downstream of the bank. The mixture becomes gradually CH_4 rich in the stream-wise direction near the outlet. The close-up concentration contours clearly illustrate the presence of concentration polarization region near the boundary layer is detached from the hollow fiber surface at both flow rates, as depicted in Figure 10 and Figure 11. Tighter spacing of the hollow fiber membranes does not influence the characteristics of the concentration profiles near surfaces, as seen in Figure 12 and Figure 13 for S/d = 2.5.

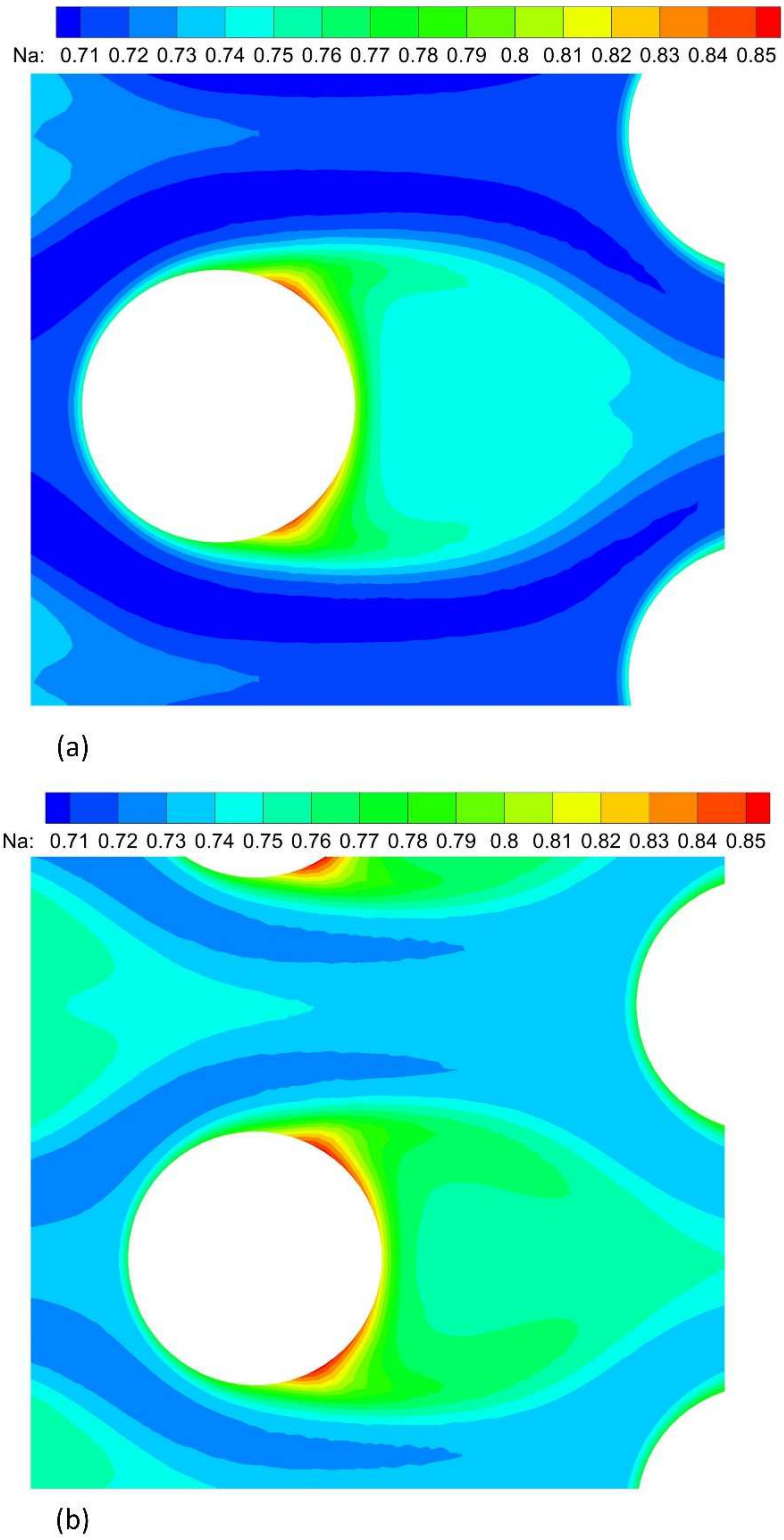

Figure 10: Mole fraction contours in the staggered geometry for *Re* = 200 and *S/d*=2 near two hollow fiber membranes: (a) AL and (b) AW.

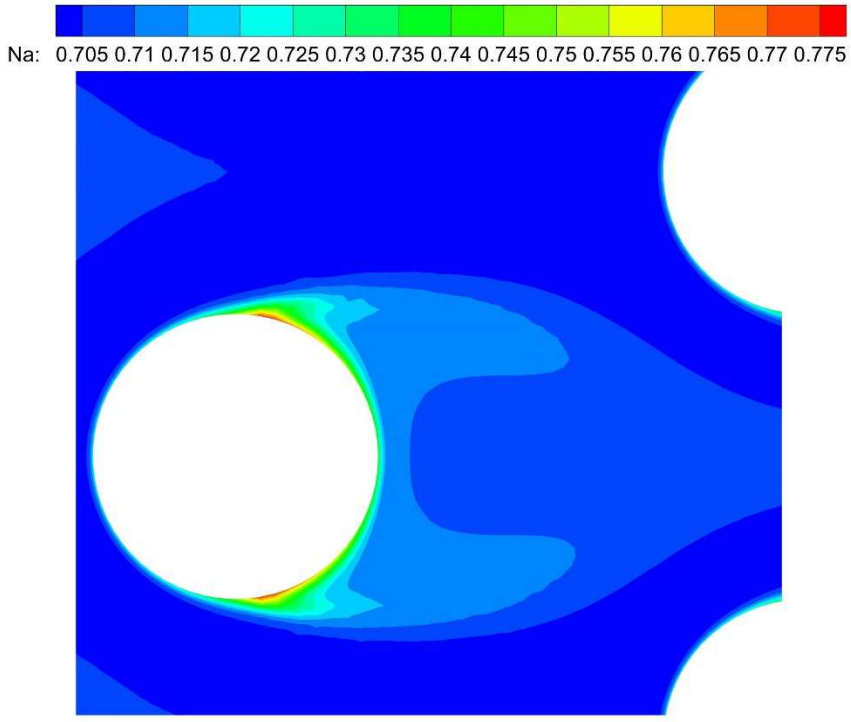

Figure 11: Mole fraction contours in the staggered geometry for *Re* = 1000 and *S/d*=2 near two hollow fiber membranes: (a) AL and (b) AW

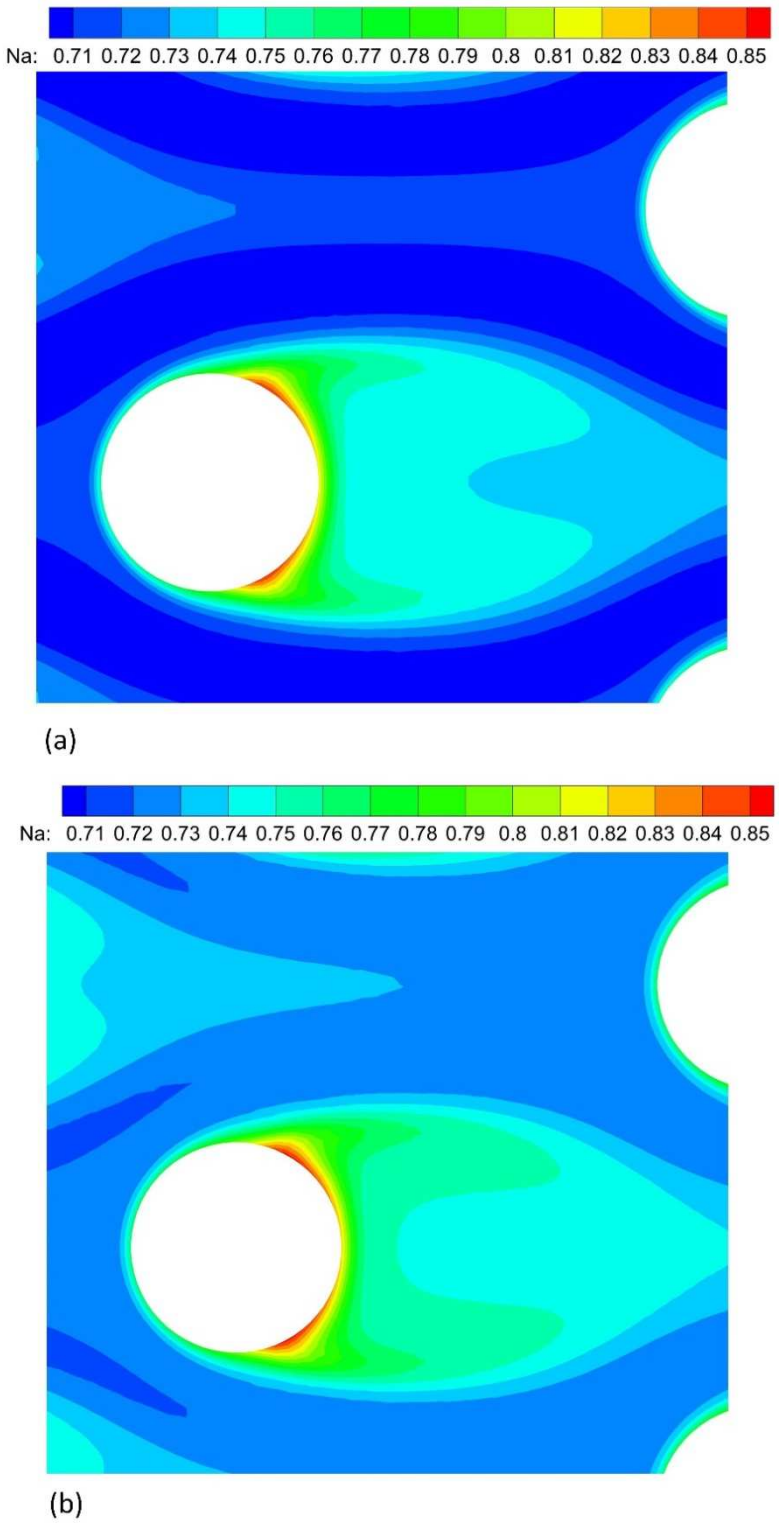

Figure 12: Mole fraction contours in the staggered geometry for *Re* = 200 and *S/d*=2.5 near two hollow fiber membranes: (a) AL and (b) AW

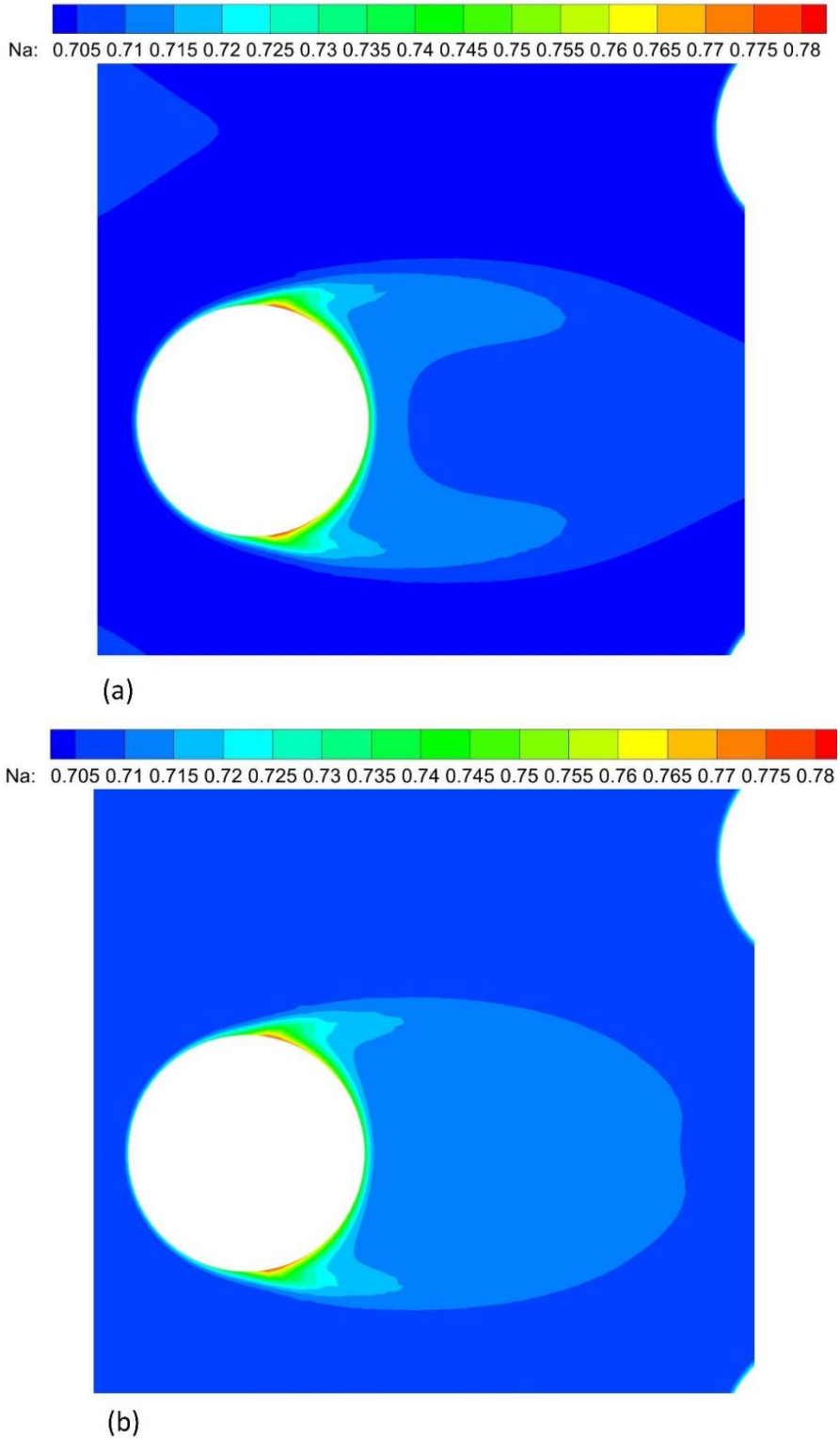

Figure 13: Mole fraction contours in the staggered geometry for *Re* = 1000 and *S/d*=2.5 near two hollow fiber membranes: (a) AL and (b) AW

The suction rate along several hollow fiber membranes is calculated for the inline and the staggered geometry. The suction rate for the representative hollow fiber membranes is plotted as a function of angle along the surface. $\theta = 0$ denotes the forward stagnation point while $\theta = \pi$ denotes the backward stagnation point. The region $0 \leq \theta \leq \pi$ represents upper section of the hollow fiber surface and the region $\pi \leq \theta \leq 2\pi$ the lower section of the surface. The profiles of the suction rate are illustrated in Figure 14 for $Re = 200$ and 1000 and $S/d = 2$ for the representative hollow fibers. The hollow fiber membranes along which the suction profiles are plotted are depicted in Figure 14a. The suction rate in each geometry decreases gradually for the hollow fibers situated downstream, as illustrated in Figure 14. The suction rate along the membrane increases as *Re* is increased in both geometries. For both flow rates hollow fiber membranes arranged in the staggered geometry have higher suction rate compared to those in the inline geometry. The suction rate is the lowest in both geometries where boundary layer is detached from the surface of the hollow fiber. The angle at which the boundary layer detached approaches to $\pi/2$ as the flow rate increases. As illustrated in Figure 14, the suction rate assumes lowest value in the region close to $\pi/2$ and $3\pi/2$ in the staggered geometry. The suction rate is much lower in the wake behind the hollow fiber membrane in the staggered geometry and it is the highest in the region near the forward stagnation region, as shown in Figure 14. On the other hand, the suction rate is low in regions near the forward and the backward stagnation point for the hollow fibers in the inline geometry. The suction rate profiles clearly shows that flow characteristics in the hollow fiber membrane bank directly influence the performance of the separation

module. It is also noticed that for the suction rate upper and lower section of the hollow fiber membrane is nearly the same in both geometries, as shown in Figure 14.

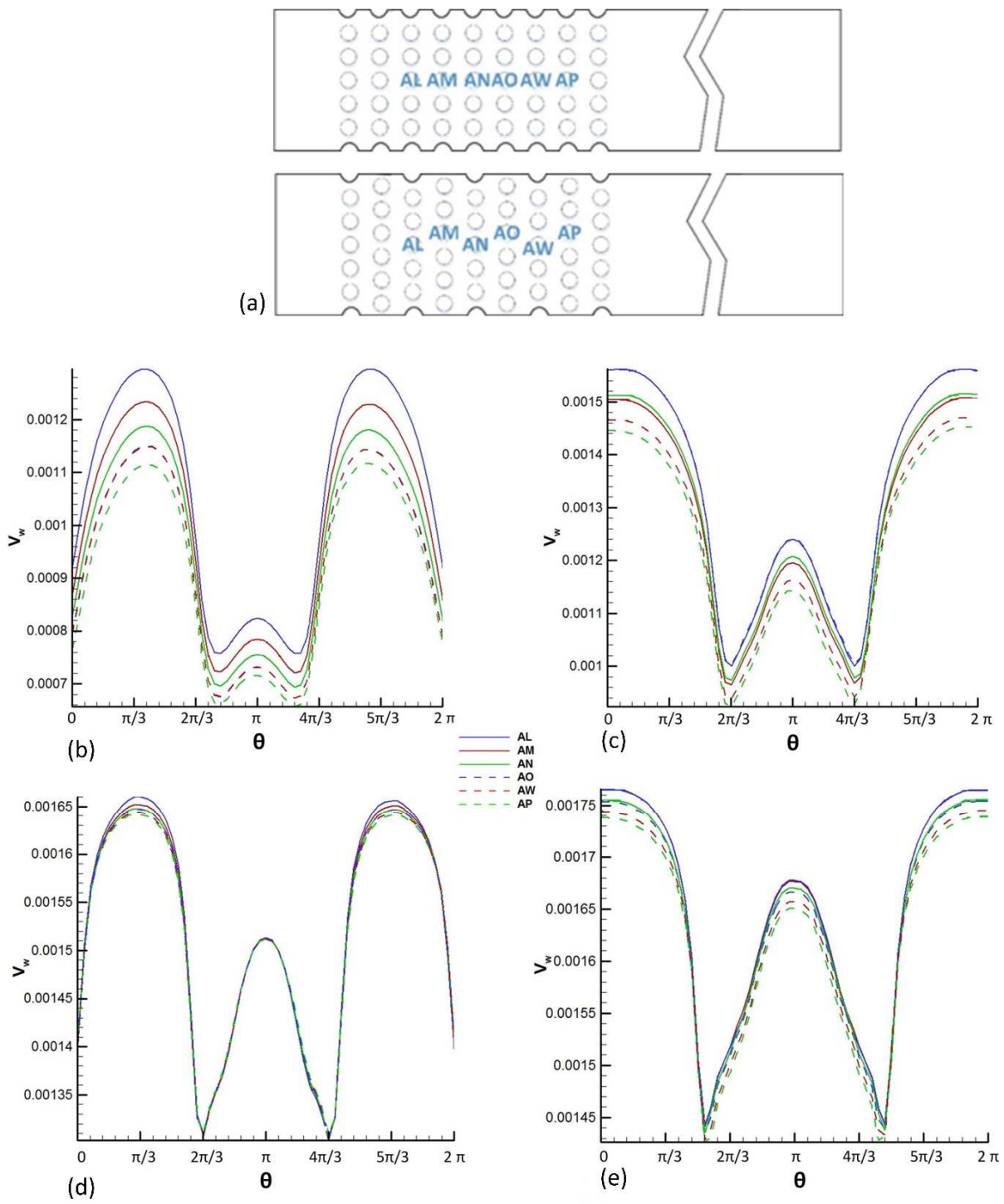

Figure 14: Profiles are shown for (a) six different hollow fiber membrane as shown in the schematic. The suction rate along the membrane at (b,c) *Re*=200 and (d,e) *Re* = 1000 for (b,d) in the inline geometry (c,e) in the staggered geometry.

The Sherwood number profiles for the hollow fibers labeled in Figure 14a are calculated for $Re = 200$ and 1000 and $S/d = 2$ and are illustrated in Figure 15 for both inline and staggered geometries. The Sherwood number profiles are plotted as a function of angle (θ) along the surface of hollow fiber membranes. The Sherwood number decreases in the flow direction in both geometries. The level of decrease is much greater in the inline geometry compared to that in the staggered geometry for both flow rates. It is also noted that the decrease in the Sherwood number in the stream-wise direction in both geometries is much less at higher flow rate. The decrease in the Sherwood number is only obtained in the region near forward stagnation point in the staggered geometry, as shown in Figure 15. Sherwood number profiles display a similar trend along the surface of the hollow fiber membrane. The maximum value of the Sherwood number occurs near the forward stagnation point and the minimum value is assumed in the region near the boundary layer is detached. The Sherwood number is lower in the wake of the hollow fiber membrane. The Sherwood number increases drastically as the flow rate is increased in both geometries. Also, it should be noticed that the Sherwood number in the staggered geometry is at least two-fold greater compared to that in the inline geometry at $Re = 200$ and 1000, as depicted in Figure 15. As mentioned earlier, the region near the boundary layer is detached from hollow fiber surface has profound influence on the hollow fiber membrane performance. That is the location nearby the Sherwood number and the suction rate assume minimum and that is also the location nearby the concentration polarization occurs.

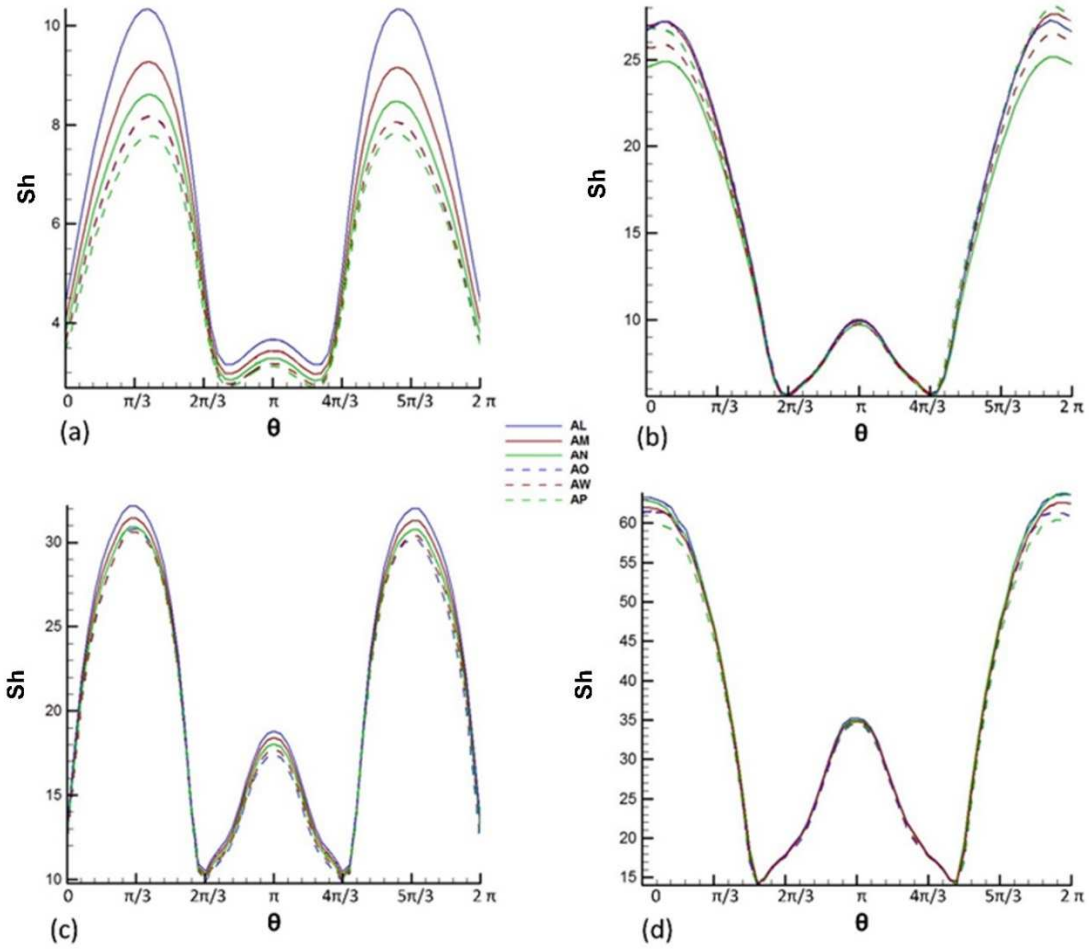

Figure 15: The local Sherwood number as a function of Θ at (a,b) *Re*=200 and at (c,d) *Re* = 1000 for (a,c) the inline geometry (b,d) the staggered geometry. Profiles are calculated for six different hollow fibers shown in the schematic of Figure 4.

The average value of the Sherwood number is calculated for the entire hollow fiber membrane bank for the inline and staggered geometry with *S/d* = 2 and *S/d* = 2.5. The average value of the Sherwood number is plotted in Figure 16 as a function of the Reynolds number. The Sherwood number increases as the Reynolds number is increased in both geometries for *S/d* = 2 and *S/d* = 2.5. The tighter spacing of the hollow fiber membrane does not alter the average value of the Sherwood number noticeably at any flow rate in the

inline geometry. On the other hand the Sherwood number increases significantly as the hollow fiber is arranged more tightly. The effect of the spacing of hollow fibers becomes more pronounced at higher *Re* in the staggered geometry, as shown in Figure 16. The Sherwood number of the staggered geometry is much greater than that of the inline geometry for both spacing at all flow rates. The difference in the Sherwood number is greater at lower values of the Reynolds number. The Sherwood number at *Re* = 200 is about three times higher in the staggered geometry compared to that in the inline geometry for both spacing, as shown in Figure 16. The arrangement of the hollow fiber membrane in the bank is essential in designing and optimizing the separation module.

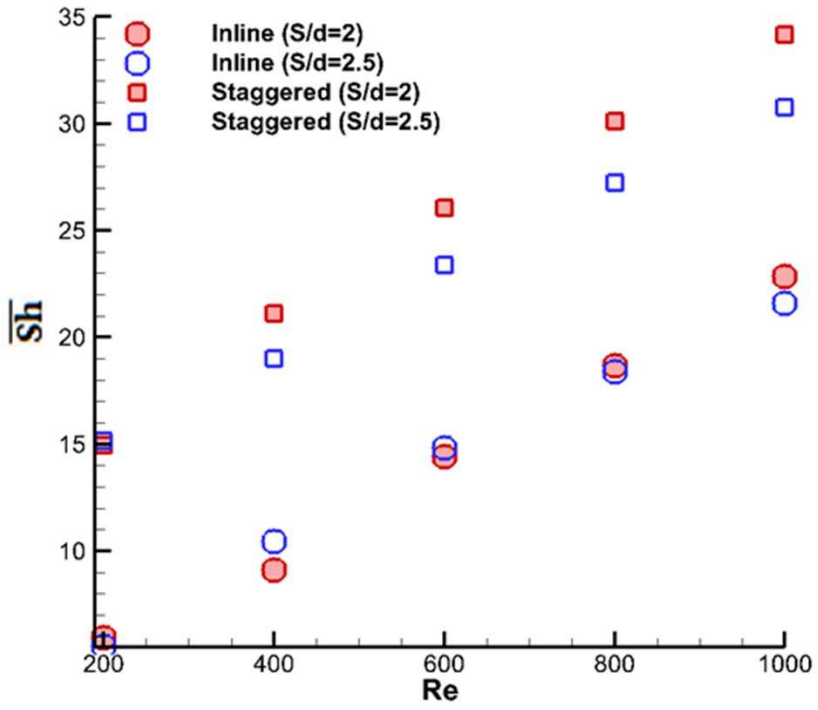

Figure 16: The average value of Sherwood number as a function of the Reynolds number for the inline and staggered geometry with *S/d* = 2 and 2.5.

The friction factor across the bank of the hollow fiber membranes is calculated for the inline and staggered geometry for both spacing. The friction factor is plotted in Figure 17 as a function of the *Re*. Energy losses are higher in the inline geometry for both spacing compared to those in the staggered geometry at all values of *Re*. Pressure drops are higher for the tighter spacing in each geometry, as shown in Figure 17. It is observed that the friction factor is not very sensitive to *Re*. Staggered arrangement of the hollow fiber membranes is more promising in terms of the energy losses.

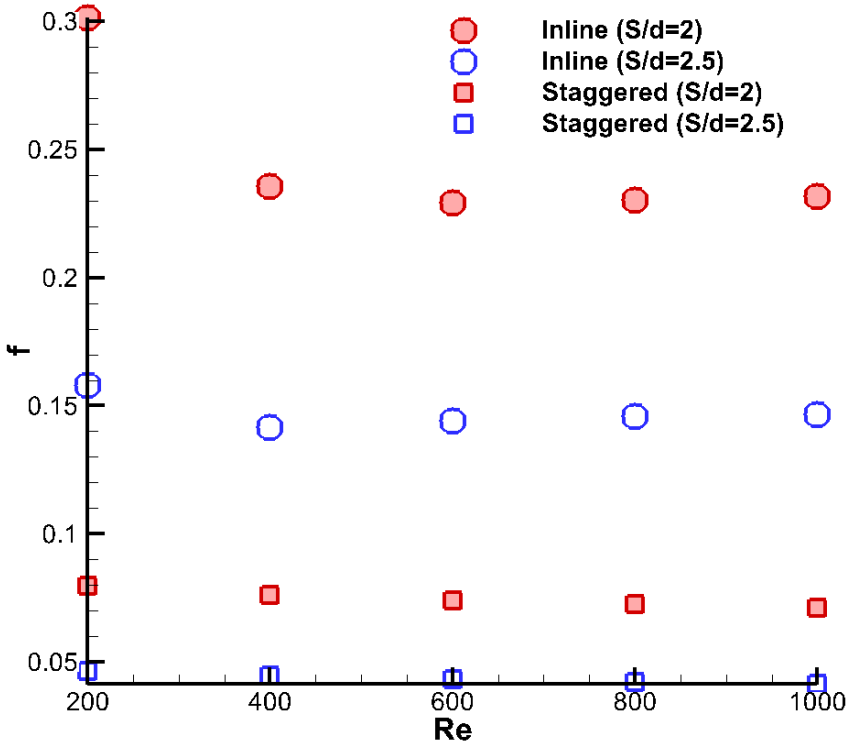

Figure 17: The friction factor for flows through the bank of hollow fibers as a function of the Reynolds number for the inline and the staggered geometry with *S/d* = 2 and 2.5.

The merit number is introduced to compare the efficiency of the inline and the staggered arrangement in the separation module. The merit number based on the enhancement of the membrane flux for the same power usage can be written as $(Sh_s/Sh_i)/(f_s/f_i)^{1/3}$, where Sh_s is the average value of the Sherwood number of the staggered geometry, Sh_i is the Sherwood number of the inline geometry, f_s is the friction factor in the staggered geometry, and f_i is the friction factor in the inline geometry. Values of the merit number are listed in Table 2 at various values of the Reynolds number for two different spacing S/d = 2 and 2.5. Merit number is calculated to be above unity at all *Re* for both spacing; implying that staggered arrangement of the hollow fiber membranes would be more efficient option compared to the inline arrangement of hollow fibers.

Re	***S/d* = 2**	***S/d* = 2.5**
200	3.927488	1.503547
400	3.374456	2.667438
600	2.631122	2.354112
800	2.369034	2.236463
1000	2.217866	2.170964

Table 2: Merit number to compare separation module containing staggered arrangement of hollow fibers and against that containing inline arrangement for *S/d* of 2 and 2.5 at various values of the Reynolds number.

5.2 Spiral wound membrane

5.2.1. Validation – transient simulations - LBM

The transient simulations are conducted in a channel containing two square cross-sectioned spacers as shown in Figure 18, using lattice Boltzmann method for *Re* =100 and 300. The lattice Boltzmann simulations are conducted by another PhD student in our research group. The channel is bounded by two impermeable walls for these simulations. The time averaged velocity and concentration field are calculated and are compared for results predicted by the steady state k-ω SST model for *Re* = 100 and 300. The boundary conditions imposed on the bounding walls and on the spacers are no-slip and no-penetration. Constant CH_4 mole fraction is used as a boundary condition for the mass transport equation on the bounding surfaces. The mole fraction at the inlet is 0.7 and at the walls it is fixed as 0.75.

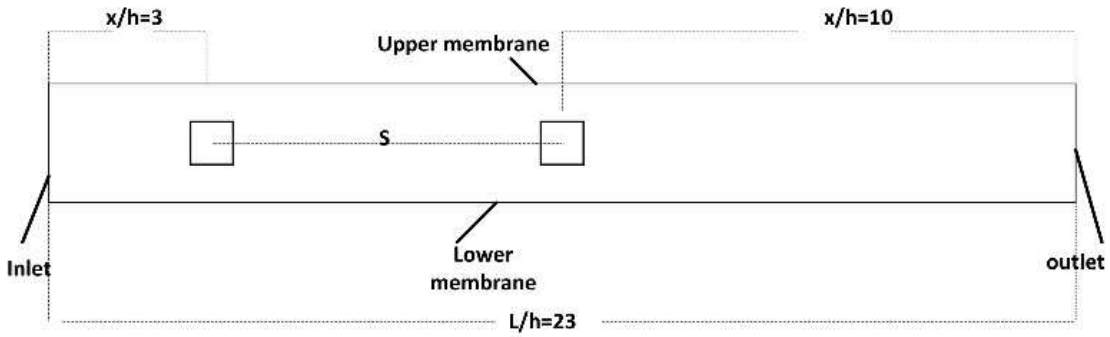

Figure 18: Schematic of the flow geometry for the lattice Boltzmann simulation.

Figures 19 and 20 show the comparison of flow profiles predicted by LBM and **k-ω** SST turbulence model at *Re* = 100 and 300. The profiles of the stream-wise component of the velocity behind the first and second spacer are depicted. The velocity profiles predicted by **k-ω** SST and LBM are nearly identical at *Re* = 100. The velocity profiles

predicted by these two methods are slightly different at *Re* = 300, however, they have the similar characteristics, as depicted in Figure 20. The deviation in the velocity profiles predicted by these methods can be attributed to the transient effect. In order to confirm these results a careful mesh optimization study needs to be conducted for both numerical methods.

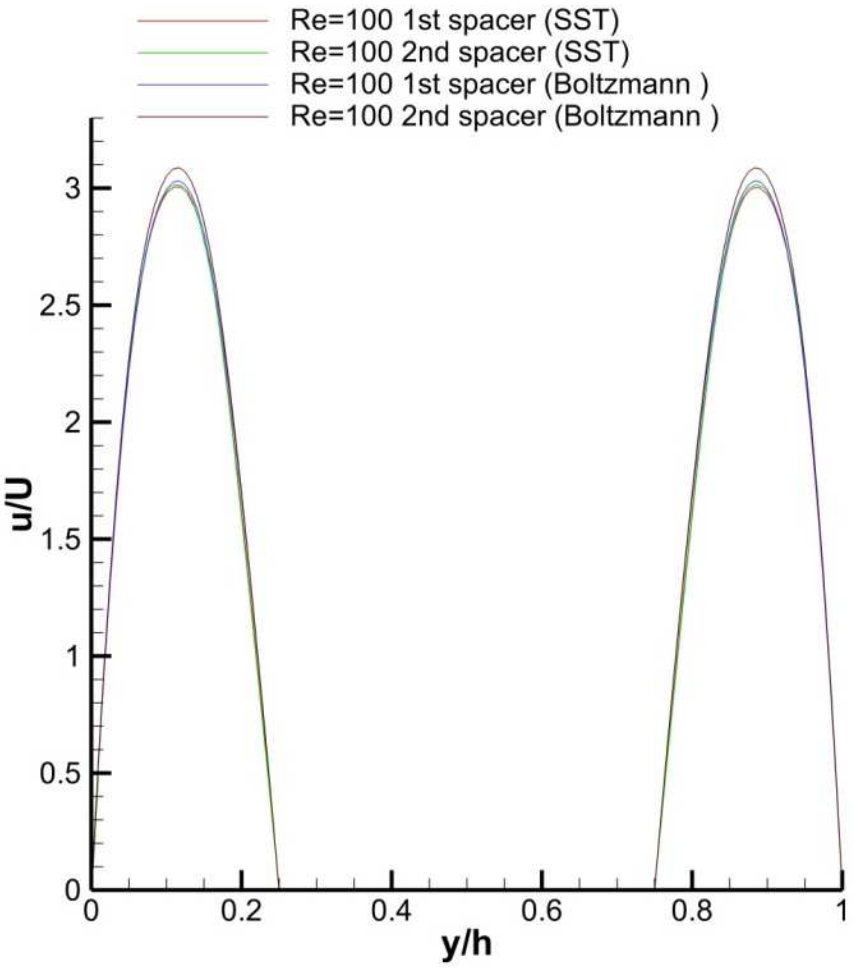

Figure 19: Velocity profiles behind the 1st and the 2nd spacer at *Re* = 100

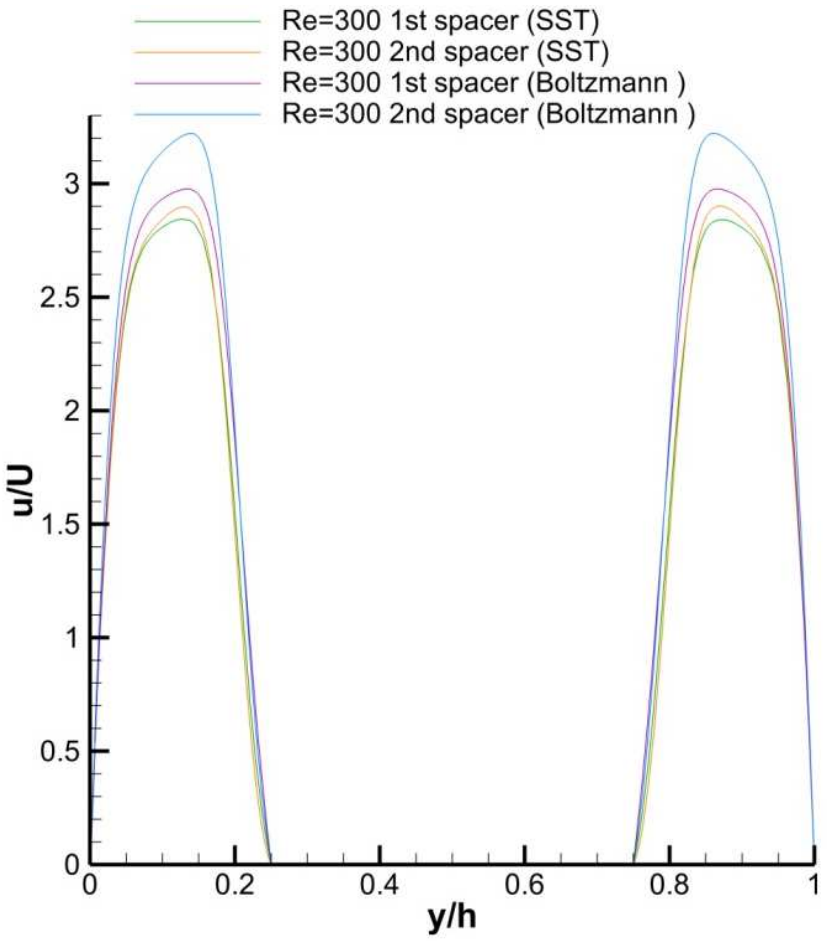

Figure 20: Velocity profiles behind the 1st and the 2nd spacer at *Re* = 300

5.2.2 Steady state simulations – k-ω SST

The steady state velocity and mole fraction profiles in a channel containing uniformly spaced seventeen spacers are obtained by employing k-ω SST turbulent model for *Re* = 300 and 500. Seventeen square cross-sectioned spacers are placed in inline arrangement at the mid-plane between the membranes as shown in Figure 2. The flow in a channel without spacers bounded by the membrane with the same properties is also simulated to provide a baseline in order to determine the influence of the spacers

on the membrane performance. Figure 21 shows the suction rate along the membrane for Re = 300 and 500, with and without the spacers. Turbulators are uniformly placed in a channel with spacing S/d_h of 10, where S is the gap between the two successive spacers and d_h is the hydraulic diameter of spacer. The suction rate increases as Re is increased along the membrane. The spacer's effect on the mass flux through the membrane is more pronounced at Re = 500. The suction rate shows a local maximum near the spacers and a local minimum near the middle point between the spacers.

Figure 22 shows the mole fraction of CH_4 as a function of x along the surface of the membrane with and without the spacers for Re = 300 and 500. The mole fraction profile displays a local maximum as the flow passes the spacer and while the local minimum is in the wake of each spacer. Although the CH_4 mole fraction on the surface of the membrane with spacers is lower compared to that without the spacer the mean value of CH_4 is higher when there are spacers in the feed channel. This indicates that CO_2 absorption by the membrane is enhanced by the turbulent mixing due to obstacles. The mixture concentration becomes richer in CH_4 when the distance from the inlet increases. Both CO_2 and CH_4 are absorbed by the membrane. The absorption of CO_2 exceeds that of the CH_4, which leads to more CH_4 mole fraction.

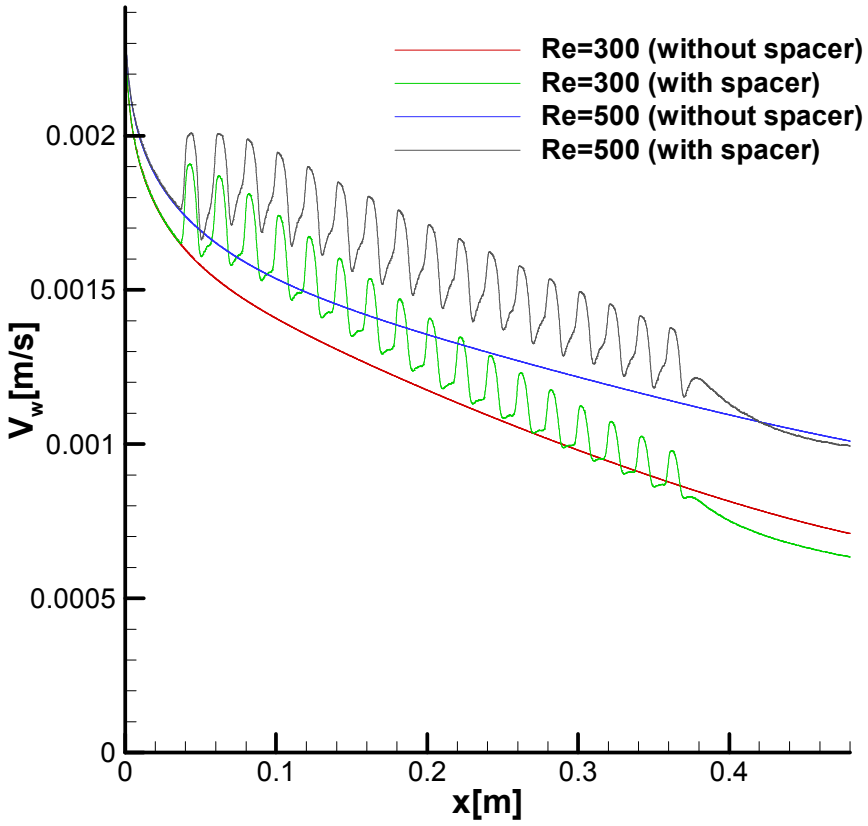

Figure 21: The suction rate along the membrane for Re=300 and 500 in a feed channel with and without spacers

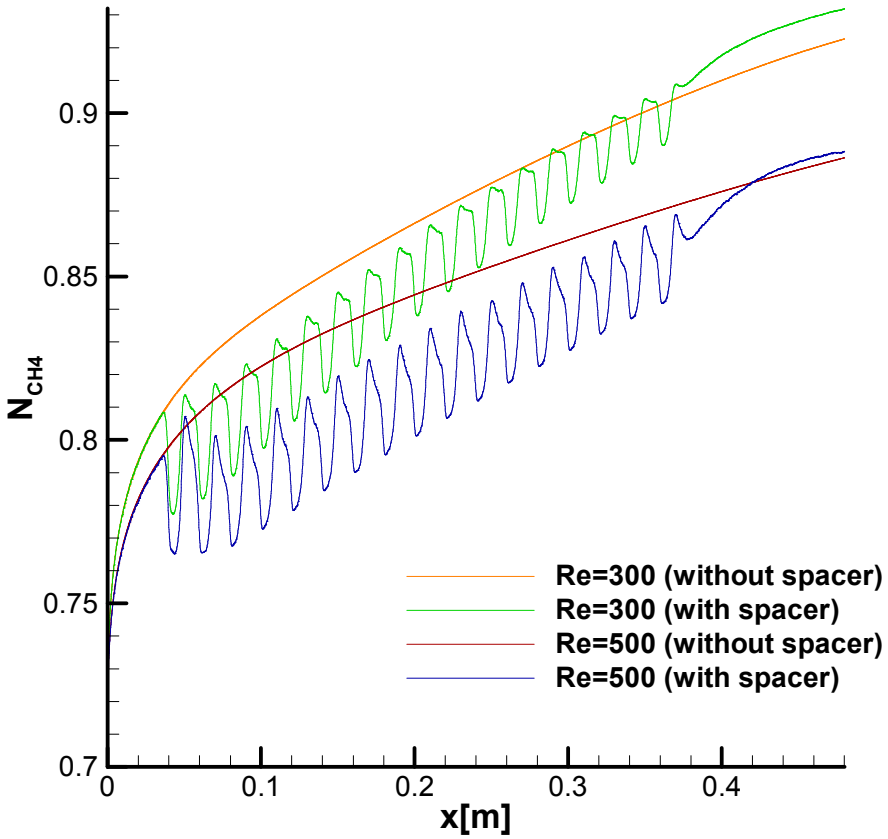

Figure 22: The mole fraction of CH_4 along the membrane for Re = 300 and 500 in a feed channel with and without spacers

6. Conclusions

The results of numerical simulations for flows over banks of hollow fiber membranes with different configurations are presented. The separation of carbon dioxide from methane in the binary mixture is studied using a separation module containing hollow fiber membranes. Surface of the hollow fiber membrane is modeled as a functional boundary where mass flux of species is determined based on the local partial pressure, the permeability, and the selectivity of the hollow fiber membrane. Velocity and the concentration field are characterized in the bank of hollow fiber membrane. The profiles

of the suction rate and the Sherwood number along the surface of the hollow fiber membranes are presented for a wide range of the Reynolds number. Staggered and inline geometry with two different spacing of hollow fiber membrane are considered. The turbulence model and the numerical method are validated by comparing predicted and measured results for flows over an impermeable cylinder. The mass flux through the membrane and the concentration polarization are greatly influenced by the local flow around the hollow fiber membranes. The suction rate is lowest and the concentration polarization is greatest in the region near the boundary layer is detached from the hollow fiber membrane surface. The amount of carbon dioxide extracted is increased and the amount of methane lost through hollow fiber membranes is reduced when hollow fibers are arranged in a staggered array. For the range of *Re* considered energy losses due to friction is less in modules containing staggered arrangement of hollow fiber membranes compared to modules containing inline arrays of hollow fibers. It is shown here that staggered arrangement of hollow fiber membranes in the gas separation modules considered is a better design. Further study is needed to optimize these systems by considering various spacing, arrangement and shape of hollow fiber membranes. It is also demonstrated here the separation module considered here can be very effective in gas separation, but the feasibility analysis is needed to determine the applicability of these systems in industrial processes. The application of these separation modules is currently studied by the present authors for desalination processes.

For spiral wound membrane, flow simulations in a channel bounded by membranes are conducted with and without the spacers. Laminar flow modeling for the flow without the spacers is used to determine the flow and concentration field. The absorption of CO_2 and

the loss of CH_4 through membrane are calculated in a channel bounded by membranes with and without spacers. The k-ω SST turbulence model is used to predict the steady state flow characteristics in the channel with an array of square cross-sectioned spacers. The turbulence model and the numerical methods are validated by comparing results obtained by lattice Boltzmann method. The comparison is performed for flow in a channel bounded by impermeable walls containing spacers. It also shows that the lattice Boltzmann method could be used to study the transient effect on the membrane performance. The presence of the spacers enhances the membrane performance at both *Re*, but the improvement is more pronounced at higher *Re* (*Re* = 500).

7. Bibliography

[1] T. Katoh, M. Tokumura, H. Yoshikawa, Y. Kawase, Dynamic simulation of multicomponent gas separation by hollow-fiber membrane module: Nonideal mixing flows in permeate and residue sides using the tanks-in-series model, Separation and Purification Technology, 76(3) (2011) 362-372.
[2] M.J. Thundyil, W.J. Koros, Mathematical modeling of gas separation permeators-for radial crossflow, countercurrent, and cocurrent hollow fiber membrane modules, Journal of Membrane Science, 125(2) (1997) 275-291.
[3] S. Lock, K. Lau, F. Ahmad, A. Shariff, Modeling, simulation and economic analysis of CO 2 capture from natural gas using cocurrent, countercurrent and radial crossflow hollow fiber membrane, International Journal of Greenhouse Gas Control, 36 (2015) 114-134.
[4] F. Ahmad, K. Lau, S. Lock, S. Rafiq, A.U. Khan, M. Lee, Hollow fiber membrane model for gas separation: Process simulation, experimental validation and module characteristics study, Journal of Industrial and Engineering Chemistry, 21 (2015) 1246-1257.
[5] S. Al-Sharif, M. Albeirutty, A. Cipollina, G. Micale, Modelling flow and heat transfer in spacer-filled membrane distillation channels using open source CFD code, Desalination, 311(0) (2013) 103-112.
[6] G. Guillen, E.M.V. Hoek, Modeling the impacts of feed spacer geometry on reverse osmosis and nanofiltration processes, Chemical Engineering Journal, 149(1–3) (2009) 221-231.
[7] S. Pal, R. Bharihoke, S. Chakraborty, S.K. Ghatak, S. De, S. DasGupta, An experimental and theoretical analysis of turbulence promoter assisted ultrafiltration of synthetic fruit juice, Separation and Purification Technology, 62(3) (2008) 659-667.
[8] M. Shakaib, S.M.F. Hasani, M. Mahmood, CFD modeling for flow and mass transfer in spacer-obstructed membrane feed channels, Journal of Membrane Science, 326(2) (2009) 270-284.
[9] A. Subramani, S. Kim, E.M.V. Hoek, Pressure, flow, and concentration profiles in open and spacer-filled membrane channels, Journal of Membrane Science, 277(1–2) (2006) 7-17.
[10] A.E. Anqi, N. Alkhamis, A. Oztekin, Numerical simulation of brackish water desalination by a reverse osmosis membrane, Desalination, 369 (2015) 156-164.
[11] M.R. Sohrabi, A. Marjani, S. Moradi, M. Davallo, S. Shirazian, Mathematical modeling and numerical simulation of CO2 transport through hollow-fiber membranes, Applied Mathematical Modelling, 35(1) (2011) 174-188.
[12] R. Kaya, G. Deveci, T. Turken, R. Sengur, S. Guclu, D.Y. Koseoglu-Imer, I. Koyuncu, Analysis of wall shear stress on the outside-in type hollow fiber membrane modules by CFD simulation, Desalination, 351(0) (2014) 109-119.
[13] S.-M. Huang, M. Yang, Heat and mass transfer enhancement in a cross-flow elliptical hollow fiber membrane contactor used for liquid desiccant air dehumidification, Journal of Membrane Science, 449 (2014) 184-192.
[14] R. Jiang, M. Yang, S. Chen, S.-M. Huang, X. Yang, Fluid flow and heat transfer across an elliptical hollow fiber membrane tube bank with randomly distributed features, International Journal of Heat and Mass Transfer, 76(0) (2014) 559-567.

[15] N. Alkhamis, A. Anqi, D.E. Oztekin, A. Alsaiari, A. Oztekin, Gas Separation Using a Membrane, in: ASME 2013 International Mechanical Engineering Congress and Exposition, American Society of Mechanical Engineers, (2013), pp. V07AT08A039-V007AT008A039.
[16] N. Alkhamis, D.E. Oztekin, A.E. Anqi, A. Alsaiari, A. Oztekin, Numerical study of gas separation using a membrane, International Journal of Heat and Mass Transfer, 80 (2015) 835-843.
[17] N. Alkhamis, A.E. Anqi, A. Oztekin, Computational study of gas separation using a hollow fiber membrane, International Journal of Heat and Mass Transfer, 89(0) (2015) 749-759.
[18] S.K. Karode, A. Kumar, Flow visualization through spacer filled channels by computational fluid dynamics I.: Pressure drop and shear rate calculations for flat sheet geometry, Journal of Membrane Science, 193(1) (2001) 69-84.
[19] D.E. Wiley, D.F. Fletcher, Techniques for computational fluid dynamics modelling of flow in membrane channels, Journal of Membrane Science, 211(1) (2003) 127-137.
[20] J.P.G. Villaluenga, Y. Cohen, Numerical model of non-isothermal pervaporation in a rectangular channel, Journal of Membrane Science, 260(1–2) (2005) 119-130.
[21] S. Ma, L. Song, Numerical study on permeate flux enhancement by spacers in a crossflow reverse osmosis channel, Journal of Membrane Science, 284(1–2) (2006) 102-109.
[22] G.A. Fimbres-Weihs, D.E. Wiley, D.F. Fletcher, Unsteady Flows with Mass Transfer in Narrow Zigzag Spacer-Filled Channels: A Numerical Study, Industrial & Engineering Chemistry Research, 45(19) (2006) 6594-6603.
[23] G.A. Fimbres-Weihs, D.E. Wiley, Numerical study of mass transfer in three-dimensional spacer-filled narrow channels with steady flow, Journal of Membrane Science, 306(1–2) (2007) 228-243.
[24] B. Marcos, C. Moresoli, J. Skorepova, B. Vaughan, CFD modeling of a transient hollow fiber ultrafiltration system for protein concentration, Journal of Membrane Science, 337(1–2) (2009) 136-144.
[25] Y. Qian, D. d'Humières, P. Lallemand, Lattice BGK models for Navier-Stokes equation, EPL (Europhysics Letters), 17(6) (1992) 479.
[26] S. Chen, G.D. Doolen, Lattice Boltzmann method for fluid flows, Annual Review of Fluid Mechanics, 30(1) (1998) 329-364.
[27] G.R. McNamara, A.L. Garcia, B.J. Alder, Stabilization of thermal lattice Boltzmann models, Journal of Statistical Physics, 81(1-2) (1995) 395-408.
[28] X. He, S. Chen, G.D. Doolen, A novel thermal model for the lattice Boltzmann method in incompressible limit, Journal of Computational Physics, 146(1) (1998) 282-300.
[29] P.L. Bhatnagar, E.P. Gross, M. Krook, A model for collision processes in gases. I. Small amplitude processes in charged and neutral one-component systems, Physical Review, 94(3) (1954) 511.
[30] P. Lallemand, L.-S. Luo, Theory of the lattice Boltzmann method: Dispersion, dissipation, isotropy, Galilean invariance, and stability, Physical Review E, 61(6) (2000) 6546.
[31] F.R. Menter, Two-equation eddy-viscosity turbulence models for engineering applications, AIAA journal, 32(8) (1994) 1598-1605.

[32] Q. Zou, X. He, On pressure and velocity boundary conditions for the lattice Boltzmann BGK model, Physics of Fluids (1994-present), 9(6) (1997) 1591-1598.
[33] C.-H. Liu, K.-H. Lin, H.-C. Mai, C.-A. Lin, Thermal boundary conditions for thermal lattice Boltzmann simulations, Computers & Mathematics with Applications, 59(7) (2010) 2178-2193.
[34] J.W. He, R. Glowinski, R. Metcalfe, A. Nordlander, J. Periaux, Active Control and Drag Optimization for Flow Past a Circular Cylinder: I. Oscillatory Cylinder Rotation, Journal of Computational Physics, 163(1) (2000) 83-117.
[35] R.D. Henderson, Details of the drag curve near the onset of vortex shedding, Physics of Fluids (1994-present), 7(9) (1995) 2102-2104.

8.VITA

Mohammed Alrehili was born on Dec. 9th ,1984. In Medina, Saudi Arabia. In 2003, Mohammed decided to study mechanical engineering at King Abdulaziz University. He graduated with a Bachelor of Science Degree in Mechanical Engineering in 2007 and right after joined The Saudi Basic Industries Corporation (SABIC) company, Hadeed Branch. He worked there as a fire system engineer for a period of three and half years. In 2011, Mohammed joined the mechanical engineering department at Tabuk University where he worked as a teaching assistant. As a part of his work contract, he have a full scholarship to pursue a graduate level degree. He joined the mechanical engineering department graduate program at Lehigh University in the summer of 2013. Mohammed was awarded his Master of Science Degree in Augest 2015.